

Energy Extraction and Particle Acceleration in String-Inspired Rotating Einstein-Maxwell-Dilaton-Axion Black Hole

Arindam Kumar Chatterjee^{a*},

^a Department of Physics, Gurukul Kangri (Deemed to be University), Haridwar - 249407, India.

Abstract

We study energy extraction and particle acceleration in the rotating Einstein-Maxwell-Dilaton-Axion (EMDA) black hole, focusing on the impact of dilaton hair $b \leq 0$ on near-horizon energetics relative to Kerr. For the Penrose process we derive analytic expressions for the maximum efficiency and show that negative b can strongly enhance the ideal gain in the extremal regime (e.g., reaching $\sim 91\%$ for $b = -0.3$). We then compute the irreducible mass M_{irr} and the corresponding rotationally extractable energy $\mathcal{E}_{\text{rot}} \equiv M - M_{\text{irr}}$, finding that M_{irr} decreases monotonically as b becomes more negative while \mathcal{E}_{rot} increases, indicating a larger spin-energy reservoir; at extremality the extracted share from rotation is $\mathcal{E}_{\text{rot}}/M \simeq 0.63$ for EMDA, reducing to the Kerr value $\simeq 0.29$ at $b = 0$. Kinematic constraints relevant to fragment production are quantified via the Wald and Bardeen–Press–Teukolsky bounds, which are progressively relaxed for more negative b . For wave superradiance we obtain the flux balance and the amplification window $0 < \beta < k\Omega_H$, with Ω_H expressed through $\Xi = r_H^2 + 2br_H + a^2$; negative b modifies Ω_H and enlarges the parameter region exhibiting negative horizon flux. Finally, we analyse two-particle collisions and derive E_{cm} , showing that the Bañados–Silk–West divergence persists at the horizon when one particle is tuned to the critical angular momentum $L_c = E/\Omega_H$, while E_{cm} remains finite for generic angular momenta. Overall, dilaton hair in EMDA simultaneously amplifies energy-extraction channels and reshapes the near-horizon thresholds governing high-energy collisions.

arXiv:2603.06273v2 [gr-qc] 19 Mar 2026

*72arindam@gmail.com

Contents

1	Introduction	2
2	The Einstein-Maxwell-Dilaton-Axion spacetime	5
3	Equations of Motion for EMDA Black Hole	8
4	Energy Extraction in EMDA Black Holes: The Penrose Process	8
4.1	The Irreducible Mass & Rotational Extraction of Energy	11
4.2	Kinematic Bounds on the Local Speeds of the Fragments	13
4.2.1	The Wald Inequality	13
4.2.2	The Bardeen-Press-Teukolsky Inequality	15
5	Superradiance of EMDA Black Hole	16
6	Centre-Of-Mass Energy Of Two Colliding Particles in the EMDA Black Hole	19
7	Discussion & Summary	28

1 Introduction

In the last decades, cosmological observations revealed that approximately 95% of our universe is made of dark energy and dark matter. Until today, the true nature of dark energy and dark matter remains an enigma. Many alternative theories have been proposed to answer this long-standing question. String theory, being one of those candidates, may provide a concrete answer and could finally solve the problem of quantum gravity. Einstein-Maxwell-Dilaton-Axion (EMDA) gravity can be understood as an effective description of the massless field content of heterotic string theory in the low-energy regime. Two scalar forces, the dilaton and the axion, are included in this model, which is a nontrivial generalisation of Einstein-Maxwell gravity and can be connected to dark energy and dark matter (see, for example (Matarrese et al., 2011)). It is widely assumed that many galaxies host supermassive black holes at their centres. Owing to the rotational dynamics of galaxies and the angular momentum carried by accreting matter, these central black holes are generally expected to possess nonzero spin, characterised by a spin parameter. Therefore, there is a lot of interest in learning more about the characteristics of these black holes, such as their mass and spin. In particular, the accumulation of astronomical data over recent decades provides compelling evidence for a supermassive black hole designated Sagittarius A* (Sgr A*) at the center of the Milky Way. According to the current cosmological paradigm, dark matter constitutes approximately 27% of the total matter-energy content of the universe. Despite the absence of direct experimental detection, a broad range of indirect observations strongly supports the existence of dark matter, as it appears to play a critical role in various astrophysical and cosmological phenomena. Prominent among these are the anomalous galactic rotation curves (Rubin et al., 1980), the dynamics of galaxy clusters (Zwicky, 2009), and the temperature anisotropies observed in the cosmic microwave background (CMB), as measured by the Planck satellite (Planck Collaboration et al., 2014). According to the celebrated singularity theorems (Penrose, 1965; Senovilla and Garfinkle, 2015; Landsman, 2022), the formation of spacetime singularities is an unavoidable consequence of classical general relativity under generic physical conditions. Nonetheless, such singularities are commonly interpreted as manifestations of the incompleteness of classical general relativity, rather than genuine physical features. In the absence of a fully developed theory of quantum gravity, significant attention has been directed toward phenomenological approaches aimed at resolving or circumventing these singularities within classical general relativity. These efforts often involve studying modified black hole solutions that exhibit regular (i.e., nonsingular) properties,

thereby offering insights into the interior structure of black holes. Consequently, an important avenue of research lies in the investigation of classical black holes and their extensions, particularly those that eliminate curvature singularities while retaining essential physical characteristics.

Arising within heterotic string theory as an effective EMDA configuration, the EMDA black hole (García et al., 1995) departs fundamentally from the classical Kerr black hole in both its theoretical origin and its spacetime structure. While the Kerr black hole is a pure solution of Einstein’s vacuum field equations, the EMDA black hole emerges from the low-energy effective action of heterotic string theory, where gravity is coupled not only to the electromagnetic field but also to two additional scalar fields—the dilaton and the axion. These extra fields modify the curvature and electromagnetic coupling of spacetime, leading to a geometry that no longer depends solely on the mass and spin of the source but also on an additional parameter associated with the dilaton charge. This alteration changes the overall causal structure, shifts the location of horizons and ergoregions, and introduces richer field interactions. Unlike the Kerr spacetime, which is asymptotically flat with a constant gravitational coupling, the EMDA spacetime features a spatially varying effective coupling influenced by the dilaton field. The presence of the axion further induces parity-violating effects and modifies the electromagnetic duality symmetry, leading to distinctive features in the electromagnetic and gravitational interactions near the black hole. Thus, the EMDA black hole represents a broader and more complex framework in which the classical Kerr geometry is recovered only as a limiting case, making it an essential model for exploring how scalar and pseudoscalar fields inherent in string-inspired theories can affect black hole structure, dynamics, and observable properties. The EMDA black hole has attracted significant interest in recent years. Jing (Jing, 1996) investigated the thermodynamic properties of the EMDA spacetime and reported several noteworthy features related to its thermodynamic stability and phase behaviour. In addition, the massless scalar quasinormal modes (QNMs) of the stationary and axisymmetric EMDA black hole were numerically evaluated by Pan (Pan and Jing, 2007) using Leaver’s continued fraction method. Their analysis yielded both the fundamental and higher-overtone quasinormal frequencies, providing valuable insights into the characteristic oscillatory and damping behaviour of scalar perturbations in this spacetime. Furthermore, the shadow structure of the EMDA black hole was examined by Wei et al. (Wei and Liu, 2013), who demonstrated that the presence of the dilaton and axion fields introduces distinctive modifications to the black hole shadows, setting it apart from the conventional Kerr case. Flathmann et al. (Flathmann and Grunau, 2015a) derived exact analytic solutions of the geodesic equations for this black hole spacetime. By separating the Hamilton-Jacobi equation, they expressed the radial and angular motions in terms of Weierstrass elliptic functions. Their analysis further classified all possible types of geodesic motion, i.e., bound, escape, and plunging orbits, and demonstrated how the dilaton and axion fields modify the orbital structure compared to the Kerr and Kerr-Newman geometries. These investigations collectively reveal that the inclusion of the dilaton charge significantly influences the system’s geometric and physical properties.

A seminal and purely classical route to extracting rotational energy from a black hole is provided by the Penrose process (Penrose and Floyd, 1971; Chandrasekhar, 1983). In this mechanical mechanism, a particle entering the ergoregion may split (or interact) so that one fragment is forced onto a negative-energy orbit as measured at infinity, while the companion escapes to infinity with a net energy gain. Such negative-energy states arise from frame dragging within the ergosphere, i.e., the region between the event horizon and the static-limit surface of the Kerr geometry, and they establish that energy extraction from a rotating black hole is, in principle, possible. The Penrose process has since been explored extensively across a broad class of spacetimes, see (Chen et al., 2025; Fatima and Abbas, 2025; Abbasi et al., 2025; Pradhan, 2019; Gupta et al., 2021; Viththani et al., 2024; Mukherjee et al., 2019; Ghosh and Sheoran, 2014; Bhat et al., 1985; Rudra et al., 2020; Parthasarathy et al., 1986a; Ganguly and SenGupta, 2014; Abdujabbarov et al., 2011a,b; Chen and Jing, 2013). Furthermore, black hole superradiance offers a second, intrinsically wave-based route to tapping the rotational

energy of a spinning horizon: for suitable field modes, the reflected wave can be amplified so that its outgoing amplitude exceeds that of the incident radiation (Pengpan, 2025; Mollicone and Destounis, 2025; Liu et al., 2024; Jha, 2024; Mukherjee et al., 2019; Menza and Nicolas, 2015; Cheriyaodathillathu et al., 2025; Herrero-Valea and Simon-Felix, 2024). The process has been explored in thermodynamic terms (Bekenstein and Schiffer, 1998; Bekenstein, 1973) and in connection with black-hole evaporation (Hawking, 1975). An even more dramatic outcome arises when the amplified bosonic field is confined and repeatedly returned to the black hole, triggering an exponential growth of the mode, commonly referred to as the black hole bomb mechanism (Press and Teukolsky, 1972; Yoshino and Kodama, 2012; Pani et al., 2012). In a broader context, superradiant instabilities have been proposed as an astrophysical probe of ultralight bosons beyond the Standard Model, such as axion-like particles, potentially leaving observable imprints relevant to dark-matter dynamics (Brito et al., 2020). Building on the foregoing motivation for energy-extraction mechanisms in black hole spacetimes, we want to examine the extent to which the heterotic string-inspired EMDA black hole can operate as an efficient particle accelerator. In this context, Bañados, Silk, and West (BSW) (Bañados et al., 2009) showed that the centre-of-mass energy of two particles freely falling from rest and colliding near the horizon of an extremal Kerr black hole can, in principle, grow without bound in the maximally rotating limit. This BSW effect has stimulated extensive interest in the prospect of ultra-high-energy collisions in strong-gravity environments, including the possibility of accessing novel phenomena at or near the Planck scale; for recent developments, see (Amir et al., 2016; Wei et al., 2010; Mukherjee et al., 2019; Pradhan, 2014; Wei et al., 2010; Liu et al., 2011; Mao et al., 2017; Amir and Ghosh, 2015; Zakria and Jamil, 2015; Feiteira et al., 2025; Ovcharenko and Zaslavskii, 2024b,a; Zhang, 2025; Rudra et al., 2020). An important issue that remains is to investigate how the presence of a dilaton parameter alters these energy extraction mechanisms and the corresponding efficiencies. As a result, these mechanisms are expected to undergo notable deviations from their classical counterparts in the Kerr spacetime. The additional coupling introduced by the dilaton field alters the local curvature and frame-dragging behaviour, thereby affecting the efficiency of energy extraction and the dynamics of particle acceleration. A particularly intriguing aspect in this context concerns the range of angular momentum for which the center-of-mass energy of colliding particles diverges, suggesting the possibility of ultra-high-energy interactions in the vicinity of the event horizon of a rotating EMDA black hole. Finally, the dilaton parameter b will be the central focus of the aforementioned study, with a detailed analysis of its role across different energy extraction schemes in the subsequent sections.

In this work, we have investigated the energy extraction schemes and particle collision in the presence of a rotating EMDA black hole. First, we establish the theoretical framework by describing the EMDA spacetime, where the dilaton hair parameter b ($b \leq 0$) is introduced as a fundamental modification to the standard Kerr geometry. We then derive the equations of motion for particles in this background, demonstrating how the parameter b alters the geodesic equations. This is followed by a detailed study of energy extraction via the Penrose Process, where we demonstrate that increasingly negative values of b significantly enhance the maximum efficiency of energy gain, particularly in the extremal regime. We subsequently compute the irreducible mass and the total rotational extraction of energy, revealing that a more negative b decreases the irreducible mass M_{irr} and expands the reservoir of extractable spin energy \mathcal{E}_{rot} compared to the Kerr limit. We further quantify the kinematic bounds on the local speeds of fragments by applying the Wald Inequality and the Bardeen-Press-Teukolsky Inequality, proving that these physical constraints on fragment production are progressively relaxed as the dilaton parameter b decreases. Additionally, we analyse the superradiance of the EMDA black hole, obtaining the flux balance equations and showing how b modifies the horizon angular velocity Ω_H to expand the frequency window for wave amplification. Finally, we investigate the center-of-mass energy (E_{cm}) of colliding particles, confirming that the Bañados-Silk-West (BSW) divergence persists at the horizon, with the parameter b determining the specific critical angular momentum thresholds required for infinite collision energy.

The paper is organised as follows. In section 2, we introduce the rotating EMDA spacetime beginning from the effective action, present the line element in Boyer-Lindquist coordinates, and summarise its basic geometric properties, including the horizon structure, ergoregion, extremality conditions, and the admissible (a, b) parameter domain. In section 3, we establish the dynamical framework by separating the Hamilton-Jacobi equation, thereby obtaining the conserved quantities and the associated radial and polar effective potentials governing geodesic motion. Section 4 is devoted to energy extraction via the Penrose process, and the maximum efficiency is reported in the extremal limit. In subsection 4.1, we compute the irreducible mass and the rotationally extractable energy $E_{\text{rot}} = M - M_{\text{irr}}$ for the EMDA black hole. In subsection 4.2, we examine the kinematic viability of the decay process by applying the Wald and Bardeen-Press-Teukolsky inequalities, from which lower bounds on fragment velocities are obtained. In section 5, we analyse superradiant scattering of a scalar field by imposing purely ingoing behaviour at the horizon and physically admissible asymptotics at infinity, leading to the relevant flux relations and the superradiant amplification condition. In section 6, we study particle acceleration via two-body collisions confined to the equatorial plane and derive the corresponding centre-of-mass energy E_{cm} . Finally, section 7 summarises our main findings and discusses their implications, thereby sharpening the phenomenology of EMDA black holes beyond Kerr. Throughout the paper we employ rescaled geometrised units with $(8\pi G = c = M = 1)$, except in the sections 4 and 5, where the black hole mass is retained explicitly for clarity.

2 The Einstein-Maxwell-Dilaton-Axion spacetime

The following action describes the four-dimensional EMDA model,

$$S = \int d^4x \sqrt{-g} \left(R - 2\partial_\mu \varphi \partial^\mu \varphi - \frac{1}{2} e^{4\varphi} \partial_\mu \kappa \partial^\mu \kappa - e^{-2\varphi} F_{\mu\nu} F^{\mu\nu} - \kappa F_{\mu\nu} \check{F}^{\mu\nu} \right), \quad (1)$$

where R denotes the scalar curvature (Ricci scalar), $F_{\mu\nu}$ is the electromagnetic field strength tensor (an antisymmetric rank-2 tensor), and $\check{F}_{\mu\nu}$ represents its Hodge dual. The scalar field φ corresponds to the dilaton scalar field, while κ denotes the axion field. The metric explicitly for EMDA black hole (Wei and Liu, 2013; Flathmann and Grunau, 2015b) can be obtained by solving the field equations derived from the action (1).

$$ds^2 = -\frac{\Delta - a^2 \sin^2 \theta}{\Sigma} dt^2 + \frac{\Sigma}{\Delta} dr^2 + \frac{(\Xi^2 - a^2 \Delta \sin^2 \theta) \sin^2 \theta}{\Sigma} d\phi^2 + \Sigma d\theta^2 - \frac{2a(\Xi - \Delta) \sin^2 \theta}{\Sigma} dt d\phi, \quad (2)$$

with the metric functions given by

$$\begin{aligned} \Sigma &= r^2 + 2br + a^2 \cos^2 \theta, \\ \Delta &= r^2 - 2mr + a^2, \\ \Xi &= r^2 + 2br + a^2. \end{aligned} \quad (3)$$

The parameter b represents the dilaton charge, while the mass parameter (m) appearing in Δ is related to the Arnowitt-Deser-Misner (ADM) mass by $M = m - b$ (equivalently $m = M + b$). The parameter a corresponds to the black hole's rotation, with angular momentum given by $J = aM$. The electric charge of the black hole is expressed as $Q = \sqrt{-2\omega b M}$, where $\omega = \exp(2\phi_0)$, ϕ_0 is the asymptotic value of the dilaton field, see (García et al., 1995). Requiring the electric charge Q to be real and assuming $M > 0$, it follows that the dilaton charge must satisfy $b \leq 0$. In the special case $b = 0$, the

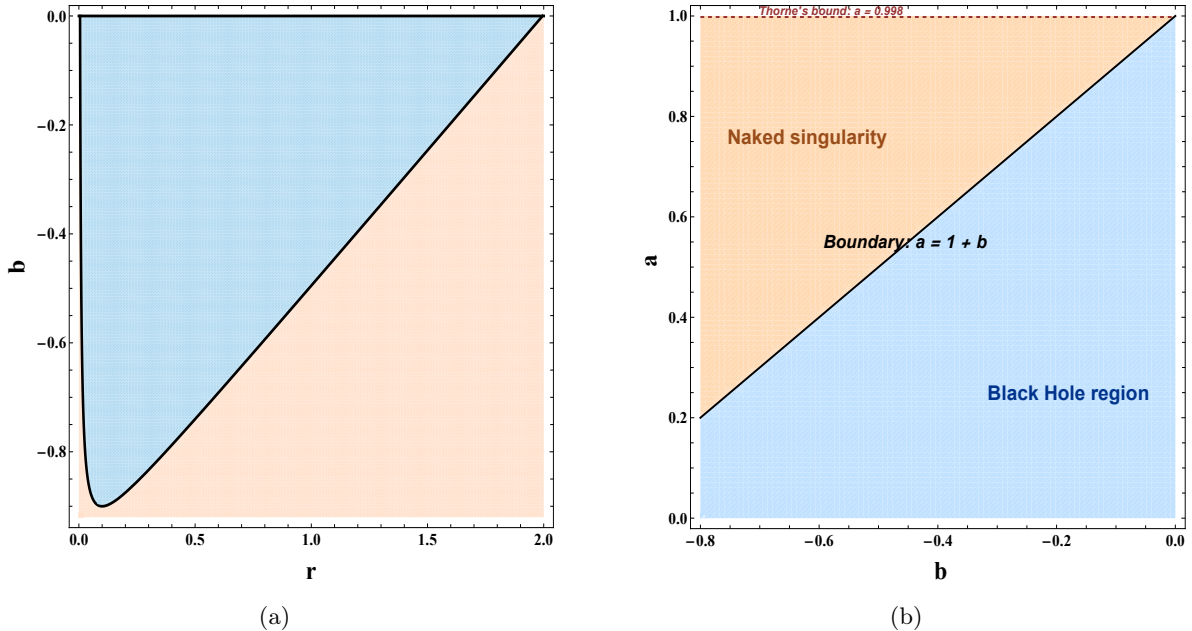


Figure 1: Panel (a) The allowed range space of the parameters b for the positive values of r . Panel (b) The range space of the parameters a and b describing a black hole and a naked singularity.

solution reduces to the standard Kerr spacetime, recovering the usual vacuum rotating black hole of GR. And in the limiting case $a = 0$, the rotating EMDA black hole solution reduces to the non-rotating Garfinkle-Horowitz-Strominger (GHS) dilaton metric (García et al., 1995; Ghosh and Mitra, 1994).

The structure of the horizons is determined by solving ($\Delta = 0$). Using ($m = M + b$), the horizon radii can be written in terms of the ADM mass M as

$$r_{\pm} = (M + b) \pm \sqrt{(M + b)^2 - a^2}. \quad (4)$$

Comprehensively, the EMDA spacetime (1) admits two horizons, obtained from the quadratic condition $\Delta = 0$. These are identified as the Cauchy horizon (r_-) and the event horizon (r_+). Unlike gauged supergravity black holes, no cosmological horizons arise here since the EMDA geometry is asymptotically flat. The outer horizon, often referred to as the surface of no return, represents the boundary beyond which no information or matter can escape to infinity. The extremal EMDA black hole corresponds to the case when the two roots of $\Delta = 0$ coincide, i.e. $r_- = r_+ = r_E$, where r_E denotes the degenerate horizon. This condition fixes a precise relation between the rotation parameter a and the dilaton parameter b (or equivalently, the ADM mass). For sub-extremal configurations ($r_+ > r_-$), the spacetime represents a regular black hole, whereas for $a^2 > (M + b)^2$ the horizons disappear and the solution reduces to a naked singularity. Thus, the transition from non-extremal to extremal, and finally to a naked singularity, is governed by the tuning of a and b . Because of the intricate interplay between these parameters, the horizon structure is best explored numerically. A useful diagnostic is the horizon separation parameter ($\delta = r_+ - r_-$), which quantifies the distance between the event horizon and the Cauchy horizon. As shown in our numerical results (see Tables 1), δ decreases as the black hole approaches the extremal limit and vanishes when $r_+ = r_-$. For astrophysical black holes, the spin parameter is subject to an upper limit, commonly referred to as Thorne's bound (Thorne, 1974), which restricts $a_{E^*} \leq 0.998$. To ensure that the horizon radii r_{\pm} are real, the condition $a^2 \leq (M + b)^2$ must be satisfied (see Table 1). Figure (1) summarises the allowed parameter space used in the analysis for the EMDA spacetime. Panel (a) shows the range of the dilaton parameter b for positive values of the radial coordinate r . This panel is used to select physically relevant

Table 1: The outer and inner horizons are represented by the radii r_{\pm} for various spin parameters a and dilaton parameters b (with $M = 1$). We also report the horizon separation $\delta = r_+ - r_-$.

b	a	r₊	r₋	δ = r₊ - r₋
-0.1	0.100000	1.7944270	0.0055728	1.7888542
	0.300000	1.7485280	0.0514719	1.6970561
	0.500000	1.6483310	0.1516685	1.4966625
	0.700000	1.4656850	0.3343146	1.1313704
	0.900000	0.9000000	0.9000000	0.0000000
-0.2	0.100000	1.5937250	0.0062746	1.5874504
	0.300000	1.5416200	0.0583802	1.4832398
	0.500000	1.4245000	0.1755002	1.2490000
	0.700000	1.1872980	0.4127017	0.7745963
	0.800000	0.8000000	0.8000000	0.0000000
-0.3	0.100000	1.3928200	0.0071797	1.3856403
	0.300000	1.3324560	0.0675445	1.2649115
	0.500000	1.1898980	0.2101021	0.9797959
	0.700000	0.7000000	0.7000000	0.0000000
-0.4	0.100000	1.1916080	0.0083920	1.1832160
	0.300000	1.1196150	0.0803848	1.0392302
	0.500000	0.9316625	0.2683375	0.6633250
	0.600000	0.6000000	0.6000000	0.0000000
-0.5	0.100000	0.9898980	0.0101021	0.9797959
	0.300000	0.9000000	0.1000000	0.8000000
	0.500000	0.5000000	0.5000000	0.0000000
-0.6	0.100000	0.7872983	0.0127017	0.7745966
	0.300000	0.6645751	0.1354249	0.5291502
	0.400000	0.4000000	0.4000000	0.0000000
-0.7	0.100000	0.5828427	0.0171573	0.5656854
	0.300000	0.3000000	0.3000000	0.0000000
-0.8	0.100000	0.3732051	0.0267949	0.3464102
	0.200000	0.2000000	0.2000000	0.0000000

configurations with $r > 0$. Panel (b) shows the (b, a) plane and separates the black hole and naked singularity regions. The diagonal curve labelled 'Boundary: $a = 1 + b'$ ' gives the extremality limit with ($M = 1$). Below this curve, spacetime admits horizons (the black hole region). Above it, the horizons disappear, and the solution corresponds to a naked singularity. The same panel also includes Thorne's bound: $a = 0.998$. This provides an astrophysical upper limit on the spin and indicates the practically relevant region of the black hole. Unlike the Kerr black hole, the presence of the dilaton parameter b permits scenarios in which both r_+ and r_- can assume negative values. Here, we focus our analysis exclusively on cases where the horizon radii are positive.

The ergoregion is defined by $g_{tt} = 0$, i.e. $(\Delta - a^2 \sin^2\theta = 0)$, which in the equatorial plane yields $r_{\text{ergo}} = 2m = 2(M + b)$. Inside it, frame dragging enforces co-rotation, forbidding retrograde motion. The curvature singularity occurs where $\Sigma = r^2 + 2br + a^2 \cos^2\theta = 0$, at which the Kretschmann scalar diverges. In the equatorial plane ($\theta = \frac{\pi}{2}$) this condition reduces to $r(r + 2b) = 0$, giving $r = 0$ and $r = -2b$. For $b < 0$, the second root lies at positive r , indicating that the singular set is not confined to $r \leq 0$ in this parametrisation. Its geometry can vary from a deformed torus to two closed surfaces depending on (a, b) (Flathmann and Grunau, 2016). Only geodesics reaching $r = 0, \theta = \frac{\pi}{2}$ terminate at the singularity; other trajectories may extend across the $r = 0$ surface into the $r < 0$ region, where

the effective gravitational interaction can become repulsive.

3 Equations of Motion for EMDA Black Hole

The geodesic structure of this spacetime has been extensively analysed in earlier works (Wei and Liu, 2013; Flathmann and Grunau, 2015b). For completeness, we briefly summarise the relevant features here, beginning with the Hamilton-Jacobi equation that governs particle motion in this black hole geometry,

$$\frac{\partial W}{\partial \alpha} = -\frac{1}{2}g^{\mu\nu} \frac{\partial W}{\partial x^\mu} \frac{\partial W}{\partial x^\nu}, \quad (5)$$

where α is an affine parameter along the geodesics and W is the Jacobi action. For this black hole spacetime (2), the Jacobi action W can be separated as

$$W = \frac{1}{2}m_0^2\alpha + L\phi + W_r(r) + W_\theta(\theta) - Et, \quad (6)$$

where W_r and W_θ are functions of r and θ , respectively. The parameters m_0 , E , and L denote the test particle's mass, energy, and angular momentum, respectively. Therefore, substituting (6) into (5), we obtain the geodesic equation,

$$\frac{dr}{d\tau} = \pm\sqrt{R}, \quad (7)$$

$$\frac{d\theta}{d\tau} = \pm\sqrt{\Theta}, \quad (8)$$

$$\frac{d\phi}{d\tau} = \frac{a(a^2E - aL + E(r^2 + 2br))}{\Sigma} + L \csc^2 \theta - aE, \quad (9)$$

$$\frac{dt}{d\tau} = \frac{\Xi(a^2E - aL + r(r + 2b)E)}{\Sigma} + aL - a^2E \sin^2 \theta, \quad (10)$$

where

$$\begin{aligned} R(r) &= (\Xi E - aL)^2 - \Delta [Q + (aE - L)^2 + m_0^2(r^2 + 2br)], \\ \Theta(\theta) &= Q - \cos^2 \theta \left[(m_0^2 - E^2)a^2 - \frac{L^2}{\sin^2 \theta} \right]. \end{aligned} \quad (11)$$

We have employed the Mino time parametrisation (Mino, 2003) as $d\alpha = \Sigma d\tau$, following the derivations presented in (Flathmann and Grunau, 2015b). Here, Q is a constant of separation, and if $b = 0$, it is just the geodesic for the Kerr black hole (Chandrasekhar, 1983).

4 Energy Extraction in EMDA Black Holes: The Penrose Process

Following the discovery of the ergosphere in rotating black holes, Roger Penrose proposed a gedanken-experiment (Penrose and Floyd, 1971) to demonstrate that the energy of a particle within the ergoregion, as measured by an observer at infinity, can become negative. He further argued that if a test particle enters the ergosphere and decays at a turning point in its geodesic trajectory into two identical fragments, one with positive energy may escape to infinity. In contrast, the other, carrying negative energy, is absorbed back by the black hole. In principle, this realisation leads to a unique way of extracting rotational energy out of a rotating black hole, hence naming it as the Penrose process. Here, we will discuss the workability of energy extraction for an EMDA black hole and the original

Penrose process, along with the further bounds from Wald and the Bardeen-Press-Teukolsky inequality. As discussed previously, in the Penrose process, a massive particle entering the ergoregion reaches a turning point ($\dot{r} = 0$) and subsequently splits into two massless fragments. From Eq. (11), we have, $R = 0$ which leads to

$$E = \frac{(\Xi - \Delta)aL \pm \sqrt{\Delta} \sqrt{(a^2 - \Xi)^2 L^2 + (\Xi^2 - \Delta a^2)(Q + m_0^2(r^2 + 2br))}}{(\Xi^2 - \Delta a^2)}, \quad (12)$$

$$L = \frac{(\Xi - \Delta)aE \pm \sqrt{\Delta} \sqrt{(\Xi - a^2)^2 E^2 + (a^2 - \Delta)(Q + m_0^2(r^2 + 2br))}}{(a^2 - \Delta)}. \quad (13)$$

The derivation of the above equations makes use of the following fundamental identity:

$$(\Xi^2 - \Delta a^2)(\Delta - a^2) = r^2(r - 2M) \left[r(r + 2b)^2 + a^2(r + 2M + 4b) \right]. \quad (14)$$

The \pm signs in Eq. (13) correspond to co-rotating and counter-rotating orbits, respectively. Referring to Eq. (12), the condition under which the energy assumes negative values, as perceived by an observer at infinity, can be derived accordingly. Without loss of generality, the normalisation $E = 1$ is adopted for a particle of unit mass initially at rest at infinity. In the present scenario, only the positive sign on the right-hand side of Eq. (12) is taken into account. Therefore, it is necessary that the following criterion be satisfied for $L < 0$, $E < 0$, and

$$(\Xi - \Delta)^2 a^2 L^2 > \Delta \left((a^2 - \Xi)^2 L^2 + (\Xi^2 - \Delta a^2)(Q + m_0^2(r^2 + 2br)) \right). \quad (15)$$

Referring to Eq. (12), we note that to ensure positive energy in the limit $a \rightarrow 0$, only the positive sign must be retained. On the other hand, for $a \neq 0$, a necessary condition for the existence of negative energy states is $L < 0$, corresponding to counter-rotating orbits with respect to the black hole's angular momentum.

Let us consider an incident massive particle of unit rest mass ($m_0 = 1$), carrying conserved energy ($E^{(c)} > 0$) and angular momentum ($L^{(c)}$), that enters the ergoregion of the EMDA spacetime while moving on the equatorial plane ($\theta = \pi/2, Q = 0$). Let the particle be broken into two massless ($m_1 = m_2 = 0$) pieces with energies and angular momenta ($E^{(a)}, L^{(a)}$) and ($E^{(b)}, L^{(b)}$) respectively, one crossing the black hole horizon while the other one comes out of the ergoregion. We have from (13)

$$\begin{aligned} L^{(c)} &= \frac{(\Xi - \Delta) a + \sqrt{\Delta} \sqrt{(\Xi - a^2)^2 + (a^2 - \Delta)(r^2 + 2br)}}{(a^2 - \Delta)} E^{(c)} = E^{(c)} \alpha^{(c)}, \\ L^{(a)} &= \frac{(\Xi - \Delta) a - \sqrt{\Delta} (\Xi - a^2)}{(a^2 - \Delta)} E^{(a)} = E^{(a)} \alpha^{(a)}, \\ L^{(b)} &= \frac{(\Xi - \Delta) a + \sqrt{\Delta} (\Xi - a^2)}{(a^2 - \Delta)} E^{(b)} = E^{(b)} \alpha^{(b)}. \end{aligned} \quad (16)$$

Using the above equations, the stationary-axisymmetric conservation laws read

$$E^{(c)} = E^{(b)} + E^{(a)}, \quad L^{(b)} + L^{(a)} = E^{(a)}\alpha^{(a)} + E^{(b)}\alpha^{(b)} = E^{(c)}\alpha^{(c)} = L^{(c)}, \quad (17)$$

which can be solved to get the energies

$$E^{(a)} = \frac{\alpha^{(c)}(r, E^{(c)}) - \alpha^{(b)}(r)}{\alpha^{(a)}(r) - \alpha^{(b)}(r)} E^{(c)}, \quad E^{(b)} = \frac{\alpha^{(a)}(r) - \alpha^{(c)}(r, E^{(c)})}{\alpha^{(a)}(r) - \alpha^{(b)}(r)} E^{(c)}. \quad (18)$$

We find using (16) we get

$$E^{(a)} = -\frac{1}{2} \left[\left(1 + \frac{(a^2 - \Delta)(r^2 + 2br)}{(\Xi - a^2)^2 (E^{(c)})^2} \right)^{1/2} - 1 \right] E^{(c)}, \quad (19)$$

$$E^{(b)} = \frac{1}{2} \left[\left(1 + \frac{(a^2 - \Delta)(r^2 + 2br)}{(\Xi - a^2)^2 (E^{(c)})^2} \right)^{1/2} + 1 \right] E^{(c)}.$$

Thus, it is clear once again that energy extraction, i.e., $E^{(b)} > E^{(c)}$ would be possible when we are inside the ergosphere (12). The amount of energy extracted is given by

$$\Delta E = E^{(b)} - E^{(c)} = \frac{1}{2} \left[\sqrt{\left(1 + \frac{(r^2 + 2br)(a^2 - \Delta)}{(\Xi - a^2)^2 (E^{(c)})^2} \right)} - 1 \right] E^{(c)}. \quad (20)$$

Consequently, the maximum of the energy extracted would correspond to when the incident particle splits at the horizon r_H , i.e. $\Delta = 0$, and we have

$$\Delta E|_{\max} = \frac{1}{2} \left[-1 + \sqrt{\left(1 + \frac{a^2}{(E^{(c)})^2 (r_H^2 + 2br_H)} \right)} \right] E^{(c)}. \quad (21)$$

Therefore, at the extremal limit ($a = a_E$, $r = r_E$), the maximum efficiency can be expressed as

$$\eta_{\max} = \frac{1}{2} \left[\sqrt{\left(1 + \frac{a_E^2}{(r_E^2 + 2br_E)} \right)} - 1 \right]. \quad (22)$$

It is customary to set the reference energy as $E^{(c)} = 1$, which serves as the normalisation condition for the analysis. It is noteworthy that this result depends explicitly on the parameters a , b and r_E . The expression retains the same formal structure as in the Kerr black hole, with the dilaton parameter b contributing implicitly via its modification of r_E . In the limiting case $b = 0$, the standard extremal Kerr result is recovered with $\eta_{\max} = 0.207$ (Chandrasekhar, 1983).

b	a_E	r_E	η_{\max}	η_{\max} (%)
0.0	1.0	1.0	0.20710678	20.710678
-0.1	0.9	0.9	0.25592895	25.592895
-0.2	0.8	0.8	0.36602540	36.602540
-0.3	0.7	0.7	0.91421356	91.421356

Table 2: Maximum efficiency η_{\max} (at extremality) computed in view of the variation of b with a_E and r_E .

Compared to a Kerr black hole, an EMDA black hole with a negative dilaton parameter b (see Figure 2) can function as a significantly more potent "rotational powerhouse." It yields substantially greater rotational energy extraction efficiency for near-extremal spin values, although this enhancement occurs

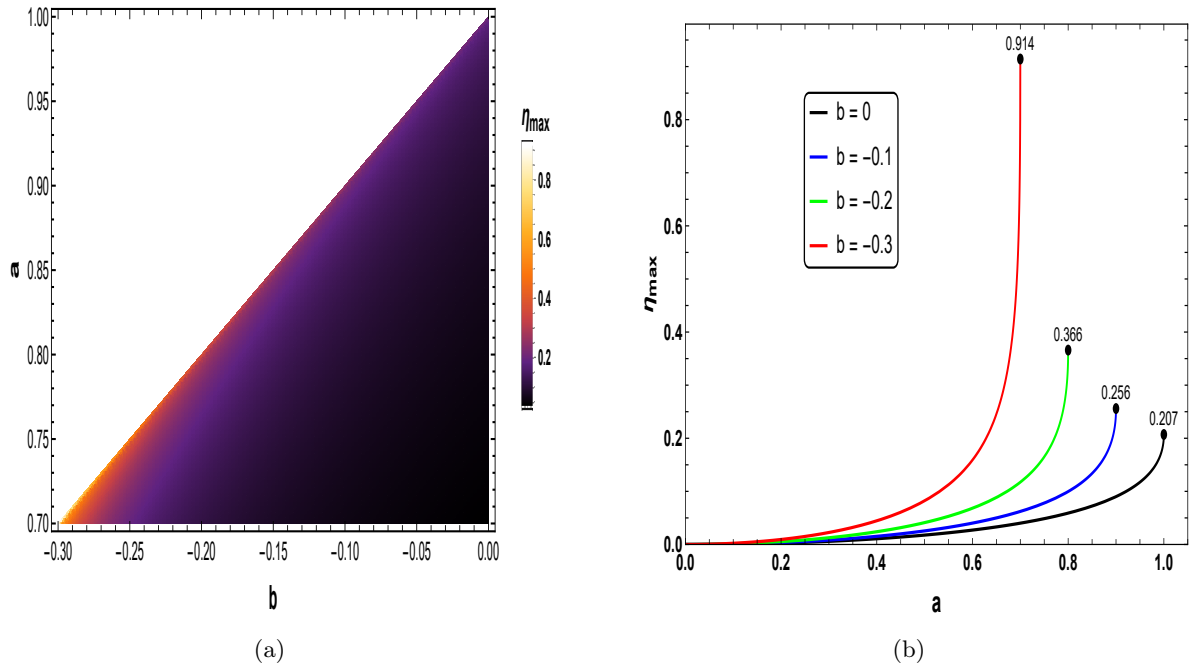


Figure 2: The efficiency of the Penrose process as a function of the parameters b and a is shown. The left panel displays the density (contour) distribution of η_{\max} in the (b, a) plane, while the right panel shows η_{\max} versus a for different values of b .

over a narrower range of admissible spins and is more sensitive to the detailed geometry of the horizon. As the extremal limit is approached, the event horizon radius r_E shifts inward with decreasing b . A specific redshift or kinematic factor constructed from r_E and the dilaton parameter b , becomes small and positive in the range $0 > b > -\frac{1}{3}$. Since the extremal spin is tied to the ADM mass ($M + b$), the numerator in the efficiency expression remains finite, while this redshift factor in the denominator becomes increasingly small. Consequently, the ratio increases significantly, and the square-root structure in Eq. (21) yields an exceptionally high value. This mechanism underlies the dramatic increase in efficiency to approximately 91% when $b = -0.3$ (see Table 2). In contrast, standard rotating solutions, including the Kerr black hole and other charged or hairy extremal black holes, fail to reach such high efficiencies under the same idealised, reversible horizon process benchmark. Their maximum efficiency values η_{\max} typically remain within $\mathcal{O}(10\%)$ to $\mathcal{O}(40\%)$, with the extremal Kerr black hole achieving only about 20.7%. Therefore, under the same theoretical constraints, such as the requirement of a real horizon and the condition that $a^2 \leq (M + b)^2$, no other known black hole solution in GR attains an efficiency comparable to the $\sim 91\%$ rotational energy yield of the EMDA black hole with $(b = -0.3)$. It should be noted, however, that real-world implementations of such processes will be tempered by factors such as back-reaction, superradiant saturation, and limitations in astrophysical matter supply. Nonetheless, the theoretical upper bound for energy extraction is significantly higher than that of Kerr-type black holes. The broader question of how much energy can be maximally extracted directly from the black hole itself as opposed to from particles orbiting it is beyond the scope of this section and will be addressed in the subsequent discussion.

4.1 The Irreducible Mass & Rotational Extraction of Energy

Through seminal contributions, Christodoulou (Christodoulou, 1970; Christodoulou and Ruffini, 1971) derived a fundamental relation connecting the total energy of a charged, rotating black hole with its irreducible mass. This result, now considered a cornerstone in black hole physics, provides deep insight into the fundamental limits of energy extraction processes from such compact objects. It is by now a well-acknowledged principle that the surface area of a black hole event horizon is non-decreasing,

a fact that underpins much of the thermodynamical interpretation of black hole mechanics. The extraction of energy from a rotating black hole results in a decrease in both its mass M and angular momentum L , leaving behind what is known as the irreducible mass, M_{irr} , of the black hole. The total mass of a black hole, also referred to as the asymptotic mass, is dependent on the observer's location. According to the newly proposed horizon mass theorem (Ha, 2007), the mass at the event horizon is always twice the irreducible mass as observed from spatial infinity. Moreover, the irreducible mass constitutes a fundamental quantity that delineates the theoretical upper bound on the extractable energy from a rotating black hole. Motivated by this remarkable framework, in the present section, we aim to extend the analogy and calculate the corresponding irreducible mass for the EMDA black hole. The irreducible mass not only reflects the intrinsic geometry of the event horizon but also integrates modifications arising from the presence of the dilaton parameter b . These contributions lead to significant corrections in the theoretical limits of energy extraction mechanisms, notably influencing the efficiency of the Penrose process.

Therefore, the irreducible mass can be defined as the component of the black hole's mass (Carroll, 2019)

$$M_{irr} = \sqrt{\frac{\mathcal{A}}{16\pi G^2}}. \quad (23)$$

The horizon area of a rotating black hole is calculated by performing the surface integral over the angular coordinates on the two-dimensional horizon cross-section at a fixed radius $r = r_+$ (Christodoulou, 1970).

$$A = \int_0^{2\pi} d\phi \int_0^\pi d\theta \sqrt{g_{\theta\theta} g_{\phi\phi}} \Big|_{r_+}, \quad (24)$$

where

$$\sqrt{g_{\theta\theta} g_{\phi\phi}} \Big|_{r_+} = \sqrt{\Sigma \cdot \frac{\Xi^2}{\Sigma} \sin^2 \theta} \Big|_{r_+} = (r_+^2 + 2br_+ + a^2) \sin \theta. \quad (25)$$

Substituting the above equation into Eq. (24) we get

$$\begin{aligned} A &= \int_0^{2\pi} \int_0^\pi (r_+^2 + 2br_+ + a^2) \sin \theta \\ &= 4\pi(r_+^2 + 2br_+ + a^2) \\ &= 8\pi(1 + 2b)r_+. \end{aligned} \quad (26)$$

Putting the above results in Eq. (23), the irreducible mass for EMDA black hole takes the form

$$M_{irr} = \sqrt{\frac{1}{2}(1 + 2b)} r_+. \quad (27)$$

Consequently, the maximum extractable energy from an extremal EMDA black hole is given by

$$\mathcal{E}_{rot} = M - M_{irr} = 1 - \sqrt{\frac{1}{2}(1 + 2b) \left((1 + b) + \sqrt{(1 + b)^2 - a^2} \right)}. \quad (28)$$

Table (3) summarises how the dilaton parameter b reshapes the reversible energy budget of the EMDA black hole. Since the horizon area fixes the irreducible mass, $M_{irr} = \sqrt{\mathcal{A}/(16\pi G^2)}$, the

\mathbf{b}	$\mathbf{a_E}$	$\mathbf{r_E}$	$\mathbf{M_{irr}}$	\mathcal{E}_{rot}	$\mathcal{E}_{\text{rot}}(\%)$
0.0	1.0000000	1.0000000	0.7071068	0.2928932	29.289322
-0.1	0.9000000	0.9000000	0.6000000	0.4000000	40.000000
-0.2	0.8000000	0.8000000	0.4898979	0.5101021	51.010205
-0.3	0.7000000	0.7000000	0.3741657	0.6258343	62.583426

Table 3: The net extractable rotational energy from an extremal EMDA black hole for different values of the dilaton parameter b is shown, where M_{irr} is the irreducible mass of the black hole.

reduction of the horizon size along the extremal EMDA family as b becomes more negative leads to a monotonic decrease of M_{irr} (Table 3). Consequently, the rotationally extractable energy defined by $\mathcal{E}_{\text{rot}} = M - M_{\text{irr}}$ increases with decreasing b . Numerically, one recovers the standard Kerr extremal value at $b = 0$, $\mathcal{E}_{\text{rot}} \simeq 0.2929$ ($\sim 29\%$) (Chandrasekhar, 1983), whereas for EMDA the extractable fraction grows to $\sim 40\%$ at $b = -0.1$, $\sim 51\%$ at $b = -0.2$, and $\sim 62.6\%$ at $b = -0.3$ (Table 3). Thus, negative dilaton hair progressively lowers the ‘irreducible’ part of the mass and enhances the maximum reversible rotational-energy reservoir beyond the Kerr bound.

4.2 Kinematic Bounds on the Local Speeds of the Fragments

We have observed so far that, for energy extraction via the Penrose process to occur, the condition $L < 0$ must be satisfied. The Wald inequality (Wald, 1974) and the Bardeen-Press-Teukolsky (Bardeen et al., 1972) inequality (see Chandrasekhar (1983)) further impose lower bounds on the speed of the ejected particles, ensuring the physical viability of the process. These inequalities serve as a fundamental theoretical tool in analysing the limits of energy extraction from rotating black holes via the Penrose process. In scenarios where a particle disintegrates within the ergoregion, its resulting fragments may carry different energy values. For energy extraction to occur, at least one of these fragments must escape to infinity with a greater total energy than that of the original particle (Parthasarathy et al., 1986b). The Wald inequality establishes an upper bound on the energy that such fragments can attain, expressed in terms of the underlying spacetime geometry. This constraint plays a pivotal role in quantifying the efficiency of energy extraction processes in rotating spacetimes and helps to elucidate both the origin and limitations of the Penrose process. Whereas the Bardeen-Press-Teukolsky inequality provides a kinematic lower bound on the local (relative) speed required for one of the particles produced in the collision to acquire negative Killing energy. In this context, we examine these inequalities within the EMDA spacetime, aiming to demonstrate that the variation in the parameter b interferes with these lower bounds. The derivations presented here closely follow those for the Kerr geometry; therefore, we omit detailed steps and refer to the cited references for a comprehensive treatment.

4.2.1 The Wald Inequality

Consider a particle (test) moving along a timelike geodesic with four-velocity u^α , satisfying the normalisation condition $u_\alpha u^\alpha = -1$, and carrying a conserved energy $\chi > 0$. Suppose this particle decays and splits into two fragments. Let σ and v^α , with $v_\alpha v^\alpha = -1$, denote the conserved energy and four-velocity, respectively, of one of the resulting particles. To analyse the process locally, we introduce an orthonormal tetrad $e_{(\mu)}^\alpha$, where indices in parentheses label the local Lorentz frame, and choose the timelike basis vector such that $u^\alpha = e_{(0)}^\alpha$. Expressing the four-velocity v^α in the basis of orthonormal frame $e_{(\mu)}^\alpha$ as $v^\alpha = e_{(\mu)}^\alpha u^{(\mu)}$, we obtain

$$v^\alpha = \frac{(u^\alpha + v^{(j)} e_{(j)}^\alpha)}{\sqrt{1 - v^{(j)} v_{(j)}}}, \quad (j = 1, 2, 3). \quad (29)$$

Now expanding the timelike killing vector $(\partial_t)^\alpha$ in the basis of orthonormal frame, we get

$$(\partial_t)^\alpha = (\partial_t)^{(0)}u^\alpha + e_{(j)}^\alpha(\partial_t)^{(j)}. \quad (30)$$

Hence, the initial particle's conserved energy $\chi = -g_{\alpha\beta}u^\alpha(\partial_t)^\beta$, can be written in terms of the orthonormal basis as

$$\chi = (\partial_t)^{(0)}. \quad (31)$$

also

$$g_{tt} = g_{\alpha\beta}(\partial_t)^\alpha(\partial_t)^\beta = (\partial_t)^{(j)}(\partial_t)_{(j)} - ((\partial_t)^{(0)})^2 = (\partial_t)^{(j)}(\partial_t)_{(j)} - \chi^2. \quad (32)$$

In a similar manner, the conserved energy (σ) associated with one of the fragments may be expressed as

$$\sigma = -(\partial_t)^\alpha v_\alpha = \frac{\chi - |\partial_t||\mathbf{v}|\cos\varphi}{\sqrt{1-|\mathbf{v}|^2}}. \quad (33)$$

In the orthonormal frame, $|\mathbf{v}|$ denotes the magnitude of the spatial part of the four-velocity, while $|\partial_t|$ represents the magnitude of the spatial projection of the timelike Killing vector field; the angle between these two vectors is denoted by φ . By substituting Eq. (32) and using the metric component ($g_{tt} = -(\Delta - a^2 \sin^2 \theta)/\Sigma$) from Eq. (2), the preceding relation can be recast as

$$\sigma = \frac{\chi - |\mathbf{v}| \left(\chi^2 - \frac{\Delta - a^2 \sin^2 \theta}{\Sigma} \right)^{1/2} \cos\varphi}{\sqrt{1-|\mathbf{v}|^2}}. \quad (34)$$

This leads to the Wald inequality (Wald, 1974) in the EMDA spacetime

$$\frac{\chi - |\mathbf{v}| \left(\chi^2 - \frac{\Delta - a^2 \sin^2 \theta}{\Sigma} \right)^{1/2}}{\sqrt{1-|\mathbf{v}|^2}} \leq \sigma \leq \frac{\chi + |\mathbf{v}| \left(\chi^2 - \frac{\Delta - a^2 \sin^2 \theta}{\Sigma} \right)^{1/2}}{\sqrt{1-|\mathbf{v}|^2}}. \quad (35)$$

Thus, in order to have a negative value of σ , we must have

$$|\mathbf{v}| > \frac{\chi}{\left(\chi^2 - \frac{\Delta - a^2 \sin^2 \theta}{\Sigma} \right)^{1/2}}. \quad (36)$$

It is evident that the lower bound discussed above attains its minimum at $\theta = \pi/2$ and at the black hole horizon, given by

$$|\mathbf{v}| > \frac{\chi}{\left(\chi^2 + \frac{a^2}{r_H^2 + 2br_H} \right)^{1/2}}. \quad (37)$$

Before the initiation of any energy-extraction process, the fragments must attain relativistic energies, as is evident from Table (4). The analysis has been further extended to include the extremal configurations, thereby ensuring a more comprehensive treatment. Thus, upon adopting the conventional normalisation $\chi = 1$, the maximum energy that a particle can sustain while remaining on a circular orbit around a maximally rotating Kerr black hole is $E_{\max} = 1/\sqrt{3}$, as reported in (Chandrasekhar, 1983). This constraint, in turn, yields a minimum velocity of $|v| = \frac{1}{\sqrt{2}}$, which is necessary to effectively initiate the Penrose process, as originally derived by Chandrasekhar (Chandrasekhar, 1983).

It is observed that EMDA black hole achieves systematically lower minimum speeds as b decreases toward $-1/3$, consistent with the same trend that yields much higher maximal extraction efficiencies in the EMDA family near that limit.

\mathbf{b}	$\mathbf{a_E}$	$\mathbf{r_E}$	$ \mathbf{v} _{\min}$
0.0	1.000000	1.000000	0.70710678
-0.1	0.900000	0.900000	0.66143783
-0.2	0.800000	0.800000	0.57735027
-0.3	0.700000	0.700000	0.35355339

Table 4: Lower bounds on the local speed $|v|_{\min}$ of the fragments for different values of the dilaton parameter b and the spin parameter a in the extremal limit.

4.2.2 The Bardeen-Press-Teukolsky Inequality

The Bardeen-Press-Teukolsky inequality (Bardeen et al., 1972) yields results analogous to those discussed above. Consider two particles with energies σ_+ and σ_- that collide at a specific spacetime point. An orthonormal basis $e_{(\mu)}^a$ is constructed as before, with the timelike vector $e_{(0)} = u^a$ representing the four-velocity of the local observer. In this locally inertial frame, we assume that the particles move with equal and opposite spatial velocities, denoted by $v^{(i)}$ and $-v^{(i)}$. The magnitude of their local relative speed in this frame can be determined using the (special) relativistic velocity addition formula. Given that the particles move with equal and opposite three-velocities, the relative speed $|v_{\text{rel}}|$ between them is given by

$$|\mathbf{v}_{\text{rel}}| = \frac{2|\mathbf{v}|}{1 + |\mathbf{v}|^2}. \quad (38)$$

Here, $|\mathbf{v}|$ denotes the magnitude of the three-velocity of each particle, as measured in the local orthonormal frame. Our objective is to determine a lower bound on the relative velocity $|\mathbf{v}_{\text{rel}}|$ such that the energy σ_- of one of the colliding particles becomes negative. By following a procedure similar to that outlined in the previous subsection, one arrives at the following result.

$$\sigma_{\pm} = \frac{(\partial_t)^{(0)} \pm |\partial_t||\mathbf{v}| \cos \varphi}{\sqrt{1 - |\mathbf{v}|^2}}. \quad (39)$$

Using the above expression, and after some algebraic manipulation, we obtain the following result,

$$(\sigma_+ + \sigma_-)^2 |\mathbf{v}|^4 - 2(\sigma_+^2 + 2g_{tt} + \sigma_-^2) |\mathbf{v}|^2 + (\sigma_+ - \sigma_-)^2 \leq 0, \quad (40)$$

which gives

$$|\mathbf{v}| \geq \frac{\sqrt{\sigma_+^2 - \left(\frac{\Delta - a^2 \sin^2 \theta}{\Sigma}\right)} - \sqrt{\sigma_-^2 - \left(\frac{\Delta - a^2 \sin^2 \theta}{\Sigma}\right)}}{(\sigma_+ + \sigma_-)}. \quad (41)$$

Considering the marginal case where $\sigma_- = 0$, we evaluate the condition on the horizon at $\theta = \pi/2$,

$$|\mathbf{v}| \geq \frac{1}{\sigma_+} \left(\sqrt{\sigma_+^2 + \frac{a^2}{r_H^2 + 2br_H}} - \sqrt{\frac{a^2}{r_H^2 + 2br_H}} \right). \quad (42)$$

Partially differentiating this with respect to r_H , we find

$$\frac{\partial |v|_{\min}}{\partial r_H} \geq \frac{a^2(r_H + b)}{(r_H^2 + 2br_H)^2} \left(\sqrt{\frac{r_H^2 + 2br_H}{a^2}} - \frac{1}{\sqrt{1 + \frac{a^2}{r_H^2 + 2br_H}}} \right) \geq 0. \quad (43)$$

\mathbf{b}	$\mathbf{a_E}$	$\mathbf{r_E}$	$ v _{\min}$	$ v _{\text{rel}}$
0.0	1.0000000	1.0000000	0.4142136	0.7071068
-0.1	0.9000000	0.9000000	0.3779645	0.6614378
-0.2	0.8000000	0.8000000	0.3178372	0.5773502
-0.3	0.7000000	0.7000000	0.1826758	0.3535533

Table 5: Minimum values of the local fragment speed ($|v|_{\min}$) and the relative speed $|v|_{\text{rel}}$ corresponding to different choices of the parameters b and a in the extremal configuration.

Finally, we once again adopt the standard choice $\sigma_+ = 1$. For the extremal Kerr black hole ($b = 0$), we obtain $|v|_{\min} \geq 0.414$, which, using Eq. (38), implies $|v_{\text{rel}}|_{\min} \geq 0.707$ (see also (Chandrasekhar, 1983)). For the extremal EMDA solution, the threshold decreases as the dilaton parameter becomes more negative; for instance, for $b = -0.3$ we find $|v|_{\min} \geq 0.183$, leading to $|v_{\text{rel}}|_{\min} \geq 0.354$ (see Table 5). Thus, a negative dilaton parameter b significantly lowers the kinematic threshold relevant for energy-extraction processes compared to the Kerr case, and this reduction becomes particularly pronounced when the spin approaches its allowed maximum for a given b .

5 Superradiance of EMDA Black Hole

The Penrose mechanism operates under the condition that the fragment escaping from a rotating black hole possesses a conserved energy greater than that of the initial particle, as described in the previous section. However, because the required astrophysical conditions are difficult to realise, the Penrose process is expected to be inefficient in realistic astrophysical environments. Superradiance, by contrast, is a wave phenomenon: although dissipation can enhance it in practical settings by providing an effective amplifier, superradiance can occur even in a vacuum provided the background spacetime is curved and admits the appropriate scattering conditions. In this sense, superradiance may be viewed as the wave analogue of the Penrose process. When an incident wave scatters off a rotating black hole, it is partially reflected and partially absorbed. Under superradiant conditions, the reflected wave emerges with enhanced amplitude, whereas the absorbed portion carries negative energy as measured by an observer at infinity.

We explore here the superradiant scattering of radiation by EMDA black hole spacetime. Let us start with the current continuity equation as we have done previously.

$$\square\Phi = \frac{1}{\sqrt{-g}}\partial_\mu(\sqrt{-g}g^{\mu\nu}\partial_\nu\Phi) = 0, \quad (44)$$

$$\Phi = e^{-i\beta t} e^{ik\phi} \vartheta(\theta) R(r). \quad (45)$$

The energy flux lost per unit time (power) takes the form as

$$dP = \beta(\beta - k\Omega_H) \left(\frac{r^2 + 2br + a^2}{\Sigma} \right)_{r_E} \iint (\Sigma)_{r_E} \Theta(\theta)^2 \sin^2\theta d\theta d\phi, \quad (46)$$

or,

$$P = \beta(\beta - k\Omega_H)[r_E^2 + 2br_E + a^2],$$

$$= \text{constant.} \quad (47)$$

Here $\Omega_H = \frac{a}{\Xi}$ is the angular velocity of the outer horizon. The superradiance is impossible if $\beta > k\Omega_H$, when P is positive. However, on the other hand, the superradiance will occur if β lies in the range $0 < \beta < k\Omega_H$. Within this range, it is clear from equation (47) that the EMDA black hole amplifies a wave mode. The angular momentum quantum number (k) must be non-zero, as it has to remove angular momentum from the black hole. Hence the energy flux lost per unit time is $P(\beta) = \Xi\beta(\beta - k\Omega_H)$, which attains its minimum at $\beta_{\min} = \frac{ka}{2\Xi}$ with value $P_{\min} = \frac{-(ka)^2}{(4\Xi)}$.

Case	Ω_H	β_{\min}	$k\Omega_H$	P_{\min}
A ($a = 0.6, b = -0.2$)	0.376260	0.376260	0.752520	-0.225756
B ($a = 0.4, b = -0.4$)	0.955546	0.955546	1.911091	-0.382218
C ($a = 0.8, b = -0.1$)	0.381144	0.381144	0.762288	-0.304915
D ($a = 0.7, b = -0.3$)	1.250000	1.250000	2.500000	-0.875000

Table 6: Superradiant flux characteristics for EMDA black holes (Cases A-D). Here $\beta_{\min} = \Omega_H$ and $P_{\min} = -(ka)^2/(4\Xi)$.

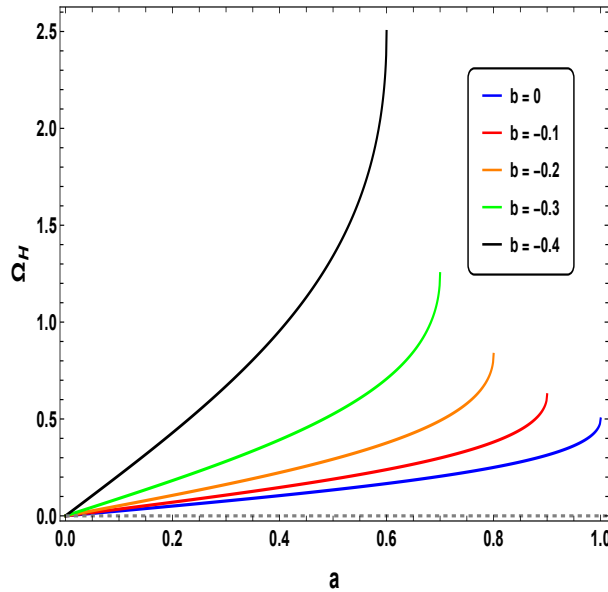


Figure 3: The behaviour of Ω_H versus a for different values of b .

A detailed comparison of the four configurations (Cases A, B, C and D) is illustrated in Figure (4). The analysis of the superradiant flux in EMDA black hole reveals a clear and systematic trend (see Table 6). The efficiency of amplification is jointly determined by the spin parameter a , the dilaton charge b , and the horizon radius r_H , through the factor $\Xi = r_H^2 + 2br_H + a^2$. In Cases A and C (see Figs. 4(a) and 4(c)), where b is only weakly negative, the horizon radius remains relatively large, giving rise to moderate values of Ω_H and consequently narrower superradiant windows $k\Omega_H \sim 0.75$. The flux minima in these cases are shallow ($P_{\min} \approx -0.23 \rightarrow -0.30$), indicating modest extraction efficiency. By contrast, Case B (Figure 4(b)) shows that increasing the negativity of b to -0.4 reduces Ξ , which boosts the angular velocity to $\Omega_H \approx 0.95$ and broadens the superradiant window nearly threefold. The corresponding dip in flux $P_{\min} \approx -0.38$ is significantly deeper, highlighting the role

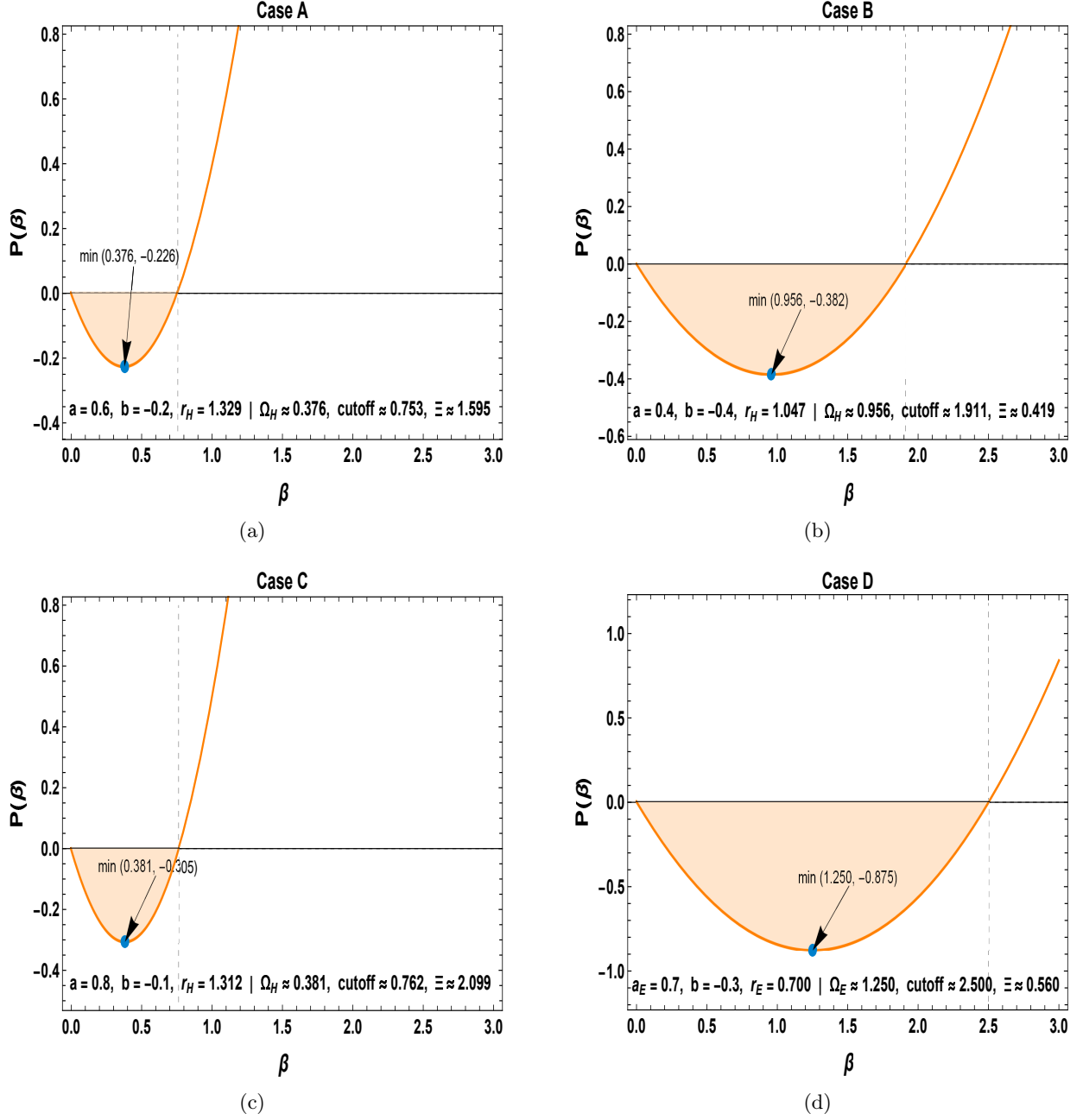


Figure 4: Superradiant flux profiles $P(\beta)$ versus β for EMDA black holes in four representative configurations: (A) $a = 0.6, b = -0.2, r_H = 1.329$; (B) $a = 0.4, b = -0.4, r_H = 1.047$; (C) $a = 0.8, b = -0.1, r_H = 1.312$; and (D) at extremality with $a_E = 0.7, b = -0.3, r_E = 0.7$. In each plot, the shaded region denotes the superradiant window $0 < \beta < k\Omega_H$, the dashed line marks the cutoff at $\beta = k\Omega_H$, and the minimum corresponds to $\beta_{\min} = \Omega_H$.

of the dilaton field in enhancing energy extraction even with lower spin. The effect culminates in Case D (Figure 4(d)), the extremal configuration at $(b = -0.3, a_E = 0.7)$, where the horizon radius shrinks to $r_E = 0.7$. This dramatically reduces Ξ , leading to a very high angular velocity ($\Omega_E = 1.25$) and the widest superradiant regime ($k\Omega_E = 2.5$), with the deepest flux minimum ($P_{\min} = -0.875$). Taken together, these results demonstrate that negative dilaton charge and proximity to extremality strongly enhance both the breadth of the superradiant band and the depth of the flux minimum. In other words, while spin alone increases efficiency, it is the combined interplay of a , b , and the resulting horizon structure that controls the overall strength of superradiance in EMDA spacetimes, with the extremal limit representing the most favourable scenario for energy extraction.

6 Centre-Of-Mass Energy Of Two Colliding Particles in the EMDA Black Hole

In a seminal study, Bañados, Silk, and West (Bañados et al., 2009) examined the collision of two particles in the vicinity of a Kerr black hole and proposed that a rotating black hole could effectively act as a natural particle accelerator. Their analysis revealed that the center-of-mass energy (E_{CM}) of two colliding particles in the equatorial plane can, in principle, become unbounded in the extremal limit of the black hole. This remarkable result implies that an extremal Kerr black hole can accelerate particles to energies approaching the Planck scale, opening new avenues for exploring ultra-high-energy astrophysical phenomena such as gamma-ray bursts, active galactic nuclei, and other extreme collision processes. Consequently, the BSW mechanism has garnered substantial attention (Zaslavskii, 2010, 2023; Patil and Joshi, 2011; Patil et al., 2011; Pradhan, 2014; Amir et al., 2016; Sheoran et al., 2020; Ghosh et al., 2014; Harada and Kimura, 2014; Mao et al., 2017) as a fundamental framework for understanding high-energy particle interactions and energy extraction in the strong-gravity regime of rotating black holes. In particular, Hussain (Hussain, 2012) argued qualitatively without detailed development that for an extremal EMDA black hole the center-of-mass energy of a collision between two uncharged particles remains finite. Furthermore, when the spin parameter and the dilaton parameter take their maximal values, the center-of-mass energy evaluated at the event horizon is still finite. In this limiting configuration, the horizon center-of-mass energy exhibits no explicit dependence on the black hole parameters, demonstrating that parameter extremisation does not induce any divergence in the collision energy. Here we revisit the problem with a detailed analysis and show explicitly how the dilaton parameter b governs the center-of-mass energy, establishing the dependence $E_{CM} = E_{CM}(b)$ for near-horizon extremal and non-extremal configurations. We aim to quantify the role of b in the overall process.

In this section, we examine the behaviour of the E_{CM} of colliding particles in the vicinity of a rotating EMDA black hole, particularly in the limiting case where the radial coordinate r approaches the event horizon r_H . Let us consider two particles of equal rest mass $M_1 = M_2 = M_0$ that are released from rest at infinity, such that $E_1/M_0 = E_2/M_0 = 1$. These particles approach the rotating EMDA black hole with different specific angular momenta L_1 and L_2 , and collide at some finite radial coordinate r . The motion of the two particles can be described by their respective four-momenta, each defined through the conserved energy and angular momentum in the EMDA spacetime as

$$P_i^\mu = M_i u_i^\mu, \quad (48)$$

where $u_i^\mu = \frac{dx_i^\mu}{d\tau}$ is the four-velocity of the particles ($i = 1, 2$). The center-of-mass energy (E_{cm}) of the two colliding particles is then given by

$$E_{\text{cm}}^2 = -P_i^\mu P_{i\mu}. \quad (49)$$

By substituting Eq. (48) into Eq. (49), we obtain

$$\frac{E_{\text{cm}}^2}{2M_0^2} = 1 - g_{\mu\nu} u_{(1)}^\mu u_{(2)}^\nu. \quad (50)$$

Substituting the components of $g_{\mu\nu}$, $u_{(1)}^\mu$, and $u_{(2)}^\mu$ for the spacetime considered here, the center-of-mass energy simplifies to

$$\frac{E_{\text{CM}}^2}{2M_0^2} = \frac{1}{r(2b+r)(a^2+r(r-2(1+b)))} \left(2ra^2(r+4b+1) - 2ra(1+2b)(L_1+L_2) \right. \\ \left. + r(2b-r+2)L_1L_2 + 2r(r-1)r(2b+r) - \sqrt{B_1}\sqrt{B_2} \right), \quad (51)$$

$$B_i = r \left(a^2(4b+2) - 4a(2bL_i+L_i) + L_i^2(2b-r+2) + 2(2b+1)r(2b+r) \right), \quad i = (1, 2).$$

Since E_{CM} is an invariant scalar, it represents a physical observable and does not depend on the choice of coordinates. This guarantees the accuracy of the formula given in Eq. (51) in both general relativity and special relativity with $M_0 = 1$, $M = 1$. The result obtained in Eq. (51) indicates that the parameter b has a significant influence on the E_{CM} . Notably, in the limiting case where the dilaton parameter vanishes $b = 0$, the corresponding expression for the E_{CM} reduces to the well-established result obtained for the Kerr black hole, as reported in (Bañados et al., 2009).

To determine the allowed range of angular momentum for particles colliding near the black hole's horizon, we first compute the corresponding effective potential. The radial equation governing the motion of a timelike particle along a geodesic can be expressed as

$$\frac{1}{2}(u^r)^2 + V_{\text{eff}} = 0. \quad (52)$$

The effective potential V_{eff} for EMDA black hole at the equatorial plane reads as

$$V_{\text{eff}} = -\frac{(\Xi E - aL)^2 - \Delta \left[(aE - L)^2 + m_0^2(r^2 + 2br) \right]}{2(r^2 + 2br)^2}. \quad (53)$$

Now, the condition for circular orbits of test particles in the rotating EMDA black hole spacetime is obtained by solving

$$V_{\text{eff}} = 0, \quad \text{and} \quad \frac{dV_{\text{eff}}}{dr} = 0. \quad (54)$$

For the time-like particles, $u^t \geq 0$ at the equatorial plane, the condition reads as

$$E(\Xi^2 - \Delta a^2) \geq aL(\Xi - \Sigma), \quad (55)$$

must be satisfied, as $r \rightarrow r_H$, the above condition reduced to

$$E \geq \frac{a}{\Xi} L = \frac{a}{r_H^2 + 2br_H + a^2} L = \Omega_H L, \quad (56)$$

where $\Omega_H = \frac{a}{\Xi}$ is the angular velocity of the outer event horizon. Moreover, the dependence on the dilaton parameter b is evident from the above equation.

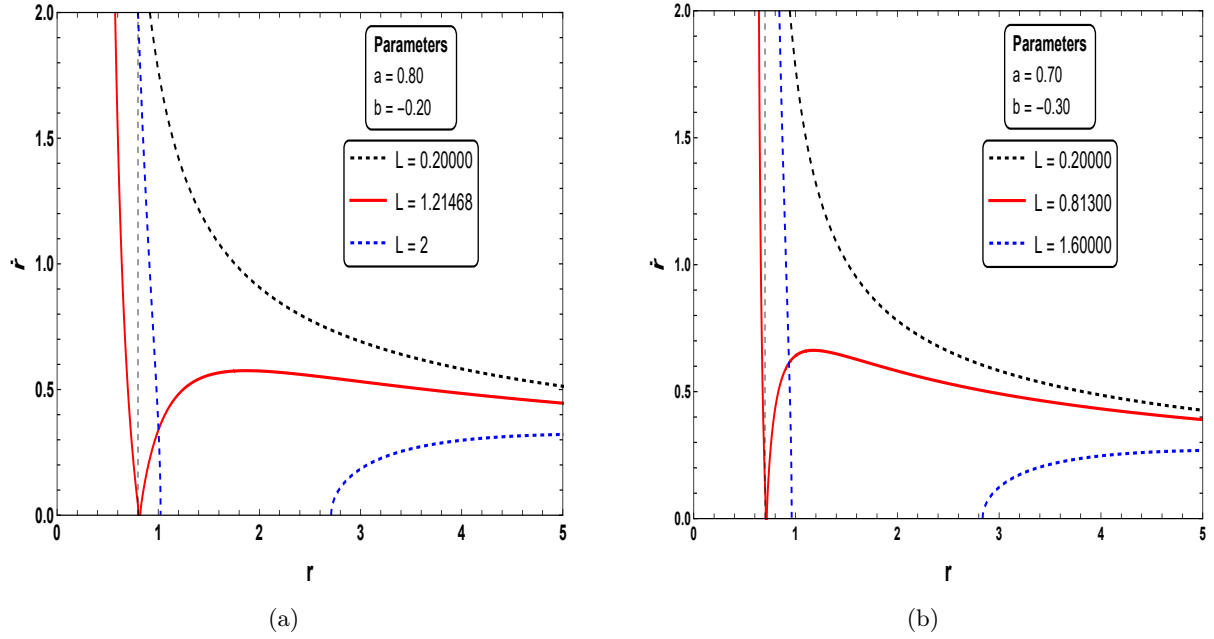


Figure 5: Illustration of the radial velocity \dot{r} versus the radial coordinate r for an extremal EMDA black hole for different values of angular momentum L , b and a . The black dotted lines correspond to $L > L_c$, the solid red line denotes $L = L_c$, and the blue dotted lines indicate $L < L_c$. The vertical dashed line denotes the location of the extremal event horizon r_E of the EMDA black hole.

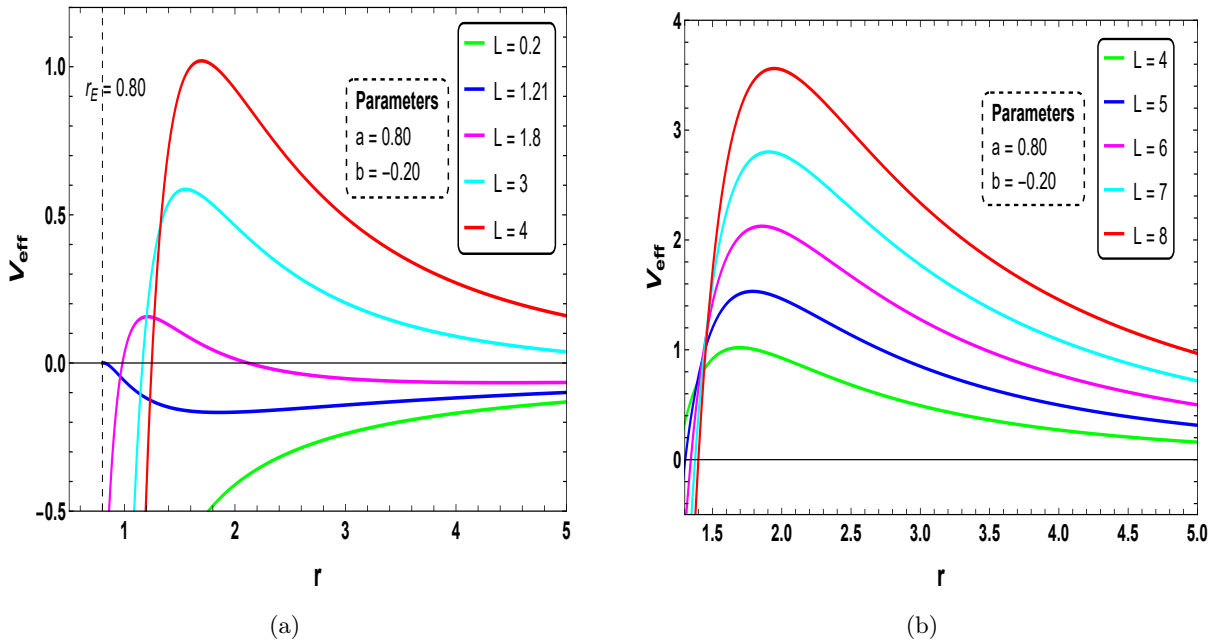


Figure 6: The behaviour of the effective potential V_{eff} versus r at the equatorial plane, showing the influence of the dilaton parameter b and rotation parameter a for different angular momenta L . Panel (i) The blue curve corresponds to L within the allowed range; Panel (ii) Where L lies outside the allowed range.

The behaviour of \dot{r} vs r is illustrated in Figure (5), for various values of the angular momentum L , spin parameter a , and dilaton parameter b . The limiting values of the angular momentum corresponding to freely falling test particles are determined from Eq. (54) for both the extremal and non-extremal cases of the EMDA black hole, and the results are presented in Tables (7) and (8). As shown in the

figures, when the angular momentum exceeds the critical value, i.e., $L > L_c$, the geodesic trajectories do not cross the event horizon, and the particles fail to fall into the black hole. Conversely, for $L < L_c$, the geodesics always fall into the black hole, indicating inevitable infall. In the limiting case where $L = L_c \equiv \frac{E}{\Omega_H}$, the particle reaches the event horizon precisely, infall occurs at that boundary. The variation of the effective potential (V_{eff}) as a function of the radial coordinate r is depicted in Figure (6) for different values of the angular momentum L . It is found that when the angular momentum of the particle lies within a specific range, the effective potential becomes negative, indicating that the particle motion is bounded within the gravitational field of the black hole. Conversely, when the angular momentum lies outside this range, the effective potential remains positive for all values of r , signifying that the particles are unbounded.

From the Table (7), it is clear that as the dilaton parameter b becomes more negative, both the effective mass and the spin of the EMDA black hole decrease, giving rise to a distinct spin-dilaton coupling. The resultant coupling shifts the event horizon inward and slightly deepens the effective potential well. In the extremal limit, the potential barrier tends to become nearly symmetric around $r = 1+b$, indicating that capture orbits can occur only for finely tuned values of the angular momentum. Consequently, prograde ($L > 0$) infall becomes increasingly restricted, whereas retrograde ($L < 0$) motion remains comparatively easier.

b	a_E	r_E	L₂(min)	L₁(max)
-0.1	0.9	0.9	-4.82	+3.04
-0.2	0.8	0.8	-4.96	+2.88
-0.3	0.7	0.7	-5.11	+2.71
-0.4	0.6	0.6	-5.25	+2.56
-0.5	0.5	0.5	-5.38	+2.41
-0.6	0.4	0.4	-5.53	+2.27
-0.7	0.3	0.3	-5.67	+2.13
-0.8	0.2	0.2	-5.81	+1.99

Table 7: The range for the numerical values of max/min angular momentum for an extremal rotating EMDA black hole with $M = 1$, $M_0 = 1$ and $E = 1$.

b	a	r₋	r₊	L₃(min)	L₄(max)
-0.1	0.710000	0.360000	1.440000	2.358947	-3.876840
-0.2	0.630000	0.320000	1.280000	1.819677	-3.059032
-0.3	0.550000	0.280000	1.120000	1.273286	-2.219859
-0.4	0.470000	0.240000	0.960000	0.709839	-1.329516

Table 8: The range for the numerical values of max/min angular momentum for a non-extremal rotating EMDA black hole with $M = 1$, $M_0 = 1$ and $E = 1$.

• **Particle collisions in the near-horizon region of an extremal EMDA black hole** — We aim to investigate the behaviour of E_{cm} as $r \rightarrow r_E$. It is observed that, in this limit, both the numerator and denominator of Eq. (51) vanish. Applying l'Hôpital's rule twice, the expression for E_{cm} as $r \rightarrow r_E$ becomes

$$\begin{aligned} \frac{E_{CM}^2}{2M_0^2} \Big|_{r \rightarrow r_E} &= C_0 + C_1(L_1 + L_2) + C_2 L_1 L_2 + \frac{G_1^2(L_2 - L_c)}{8(L_1 - L_c)^3} + \frac{G_2^2(L_1 - L_c)}{8(L_2 - L_c)^3} \\ &\quad - \frac{G_1 G_2}{4(L_1 - L_c)(L_2 - L_c)} - \frac{H_1(L_2 - L_c)}{4(L_1 - L_c)} + \frac{H_2(L_1 - L_c)}{4(L_2 - L_c)}, \end{aligned} \quad (57)$$

with coefficient

$$C_0 = \frac{26b^2 + 30b + 8}{3b^2 + 4b + 1}, \quad C_1 = 0, \quad C_2 = -\frac{1}{3b^2 + 4b + 1},$$

$$K = 4(1+b)(1+2b), \quad G_i = K(L_c - L_i), \quad H_i = 40b^2 + 44b + 12 - 2L_i^2, \quad (i = 1, 2).$$

By substituting $b = -0.2$ into the above expression, Eq. (57) reads as

$$\begin{aligned} \frac{E_{CM}^2}{2M_0^2} \Big|_{r \rightarrow r_E} &= 9.5 - 3.123 L_1 L_2 + \frac{1.92(L_c - L_1)^2(L_2 - L_c)}{8(L_1 - L_c)^3} + \frac{1.92(L_c - L_2)^2(L_1 - L_c)}{8(L_2 - L_c)^3} \\ &\quad - \frac{3.84(L_c - L_1)(L_c - L_2)}{4(L_1 - L_c)(L_2 - L_c)} - \frac{(4.8 - 2L_1^2)(L_2 - L_c)}{4(L_1 - L_c)} + \frac{(4.8 - 2L_2^2)(L_1 - L_c)}{4(L_2 - L_c)}. \end{aligned} \quad (58)$$

Where $a_E = r_E = 0.8$ and $L_c = \frac{E}{\Omega_E} = 1.2$, (see Table (7)). The above Eq. (58) represents the limiting (extremal) behaviour of the E_{CM} near the event horizon, evaluated for the specific case of a particle with the critical angular momentum L_c . It is evident from the analysis that the center-of-mass energy E_{CM} diverges (infinity) when either of the angular momenta, L_1 or L_2 , attains its critical value L_c . For all other generic values of L_1 and L_2 , the E_{CM} remains finite. The dilaton parameter b merely shifts the critical parameters r_E , Ω_E , L_c and the rate of divergence without destroying the mechanism. This observation implies that an extremal EMDA black hole can, in principle, serve as a natural particle accelerator, capable of accelerating particles to arbitrarily high energies and thereby providing a potential framework to probe Planck-scale physics. However, to achieve an infinite E_{CM} , the infalling particles must possess angular momenta within a specific critical range, as shown in Table (7).

Furthermore, Figure (7) illustrates the variation of the E_{CM} as a function of the radial coordinate r for different values of the angular momenta L_1 and L_2 , keeping the spin parameter a and the dilaton parameter b fixed. It is observed that E_{CM} diverges at the event horizon when either L_1 or L_2 attains the critical value L_c . This indicates that the critical angular momentum L_c must lie within the permissible range for which the particle can reach the black hole horizon. In Figure (8), the near-horizon variation of the center-of-mass energy, E_{CM} , as a function of the spin parameter a is presented for different choices of L_1 and L_2 , while the dilaton parameter b is kept fixed. Finally, the dependence of the E_{CM} on the dilaton parameter is illustrated in Figure (9(a)), where E_{CM} is plotted versus the radial coordinate r for different values of b , while Figure (10(a)) presents the corresponding variation of E_{CM} with the spin parameter a . For comparison, the extremal Kerr limit ($Q = 0$) is shown separately in Figs. (9(b)) and (10(b)). Jacobson (Jacobson and Sotiriou, 2010) argued that infinite center-of-mass energy can be achieved by colliding particles only after an endless amount of proper time, making such events physically unrealistic. However, in the case of a non-extremal black

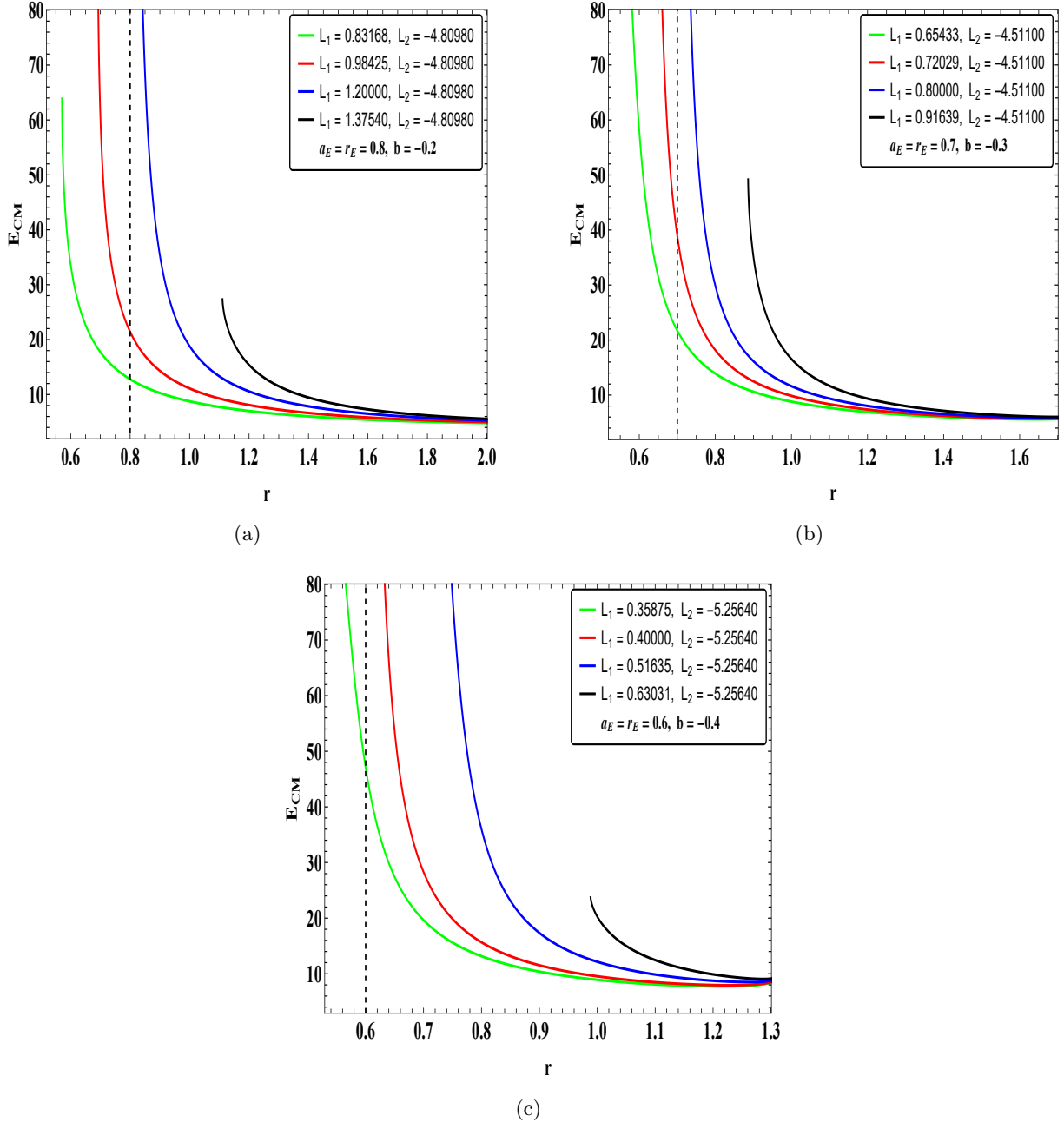


Figure 7: Variation of the center-of-mass energy E_{CM} versus r for an extremal EMDA black hole for fixed values of the dilaton parameter $b = -0.2$, $b = -0.3$ and $b = -0.4$, respectively. Each curve corresponds to different values of the angular momentum L_1 , with L_2 held constant. The vertical dashed line in each plot denotes the location of the extremal event horizon r_E of the EMDA black hole.

hole, the proper time required for a particle to reach the event horizon, though significantly large, remains finite. Therefore, it is plausible to study particle collisions near a non-extremal black hole, where such processes could occur within a physically meaningful timescale. In the next paragraph, we will explore the collision of particles near a non-extremal EMDA black hole.

• **Particle collisions in the near-horizon region of a non-extremal EMDA black hole** — Finally, we analyse the behaviour of the center-of-mass energy E_{CM} in the vicinity of the event horizon r_H^+ for a non-extremal rotating EMDA black hole. As the radial coordinate r approaches r_H^+ , both the

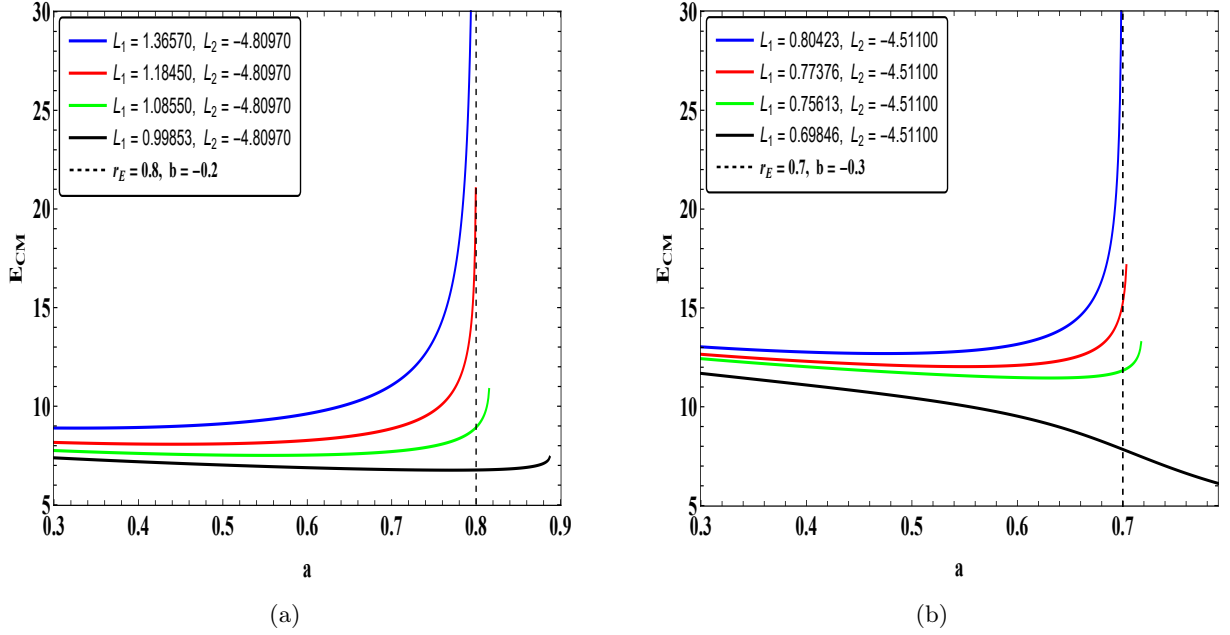


Figure 8: Variation of the center-of-mass energy E_{CM} versus a for an extremal EMDA black hole for fixed values of the dilaton parameter $b = -0.2$ and $b = -0.3$, respectively. Each curve corresponds to different values of the angular momentum L_1 , with L_2 held constant. The vertical dashed line in each plot denotes the location of the extremal event horizon r_E of the EMDA black hole.

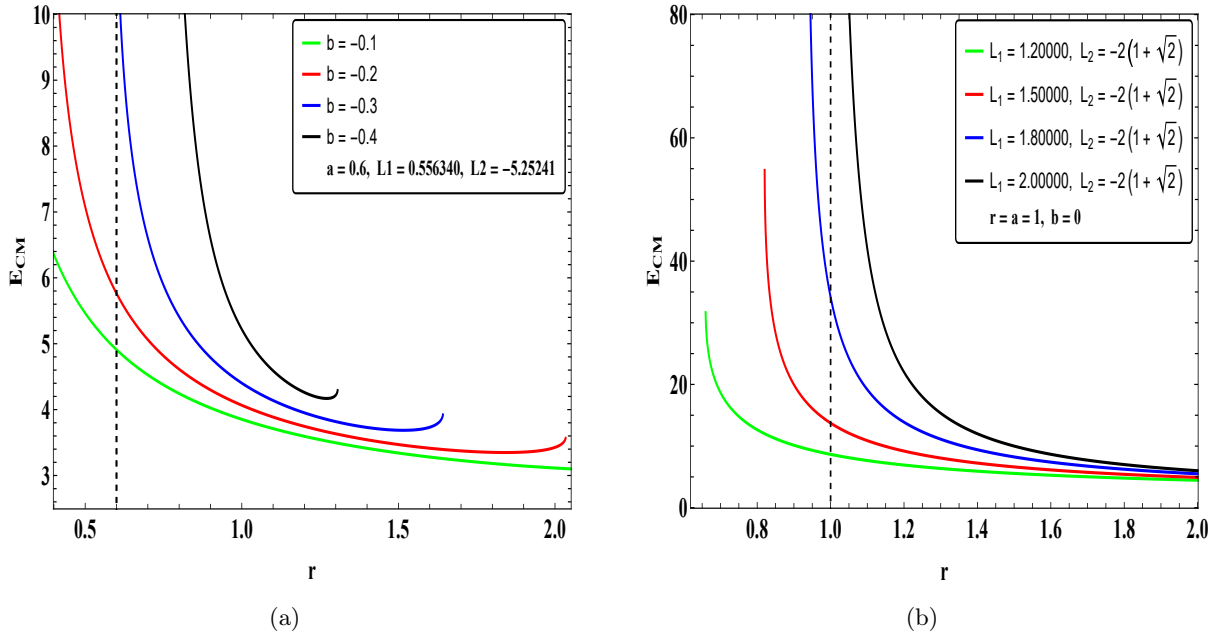


Figure 9: Variation of the center-of-mass energy E_{CM} as a function of the radial coordinate r . Panel (a) shows the EMDA case for different values of the dilaton parameter b , while panel (b) corresponds to the extremal Kerr black hole limit ($b = 0$). In both panels, the vertical line indicates the location of the event horizon.

numerator and the denominator of Eq. (51) simultaneously approach zero. To determine the limiting value E_{CM} near the event horizon under non-extremal conditions, we apply l'Hospital's rule. Finally, the expression for E_{CM} as $r \rightarrow r_H^+$ becomes

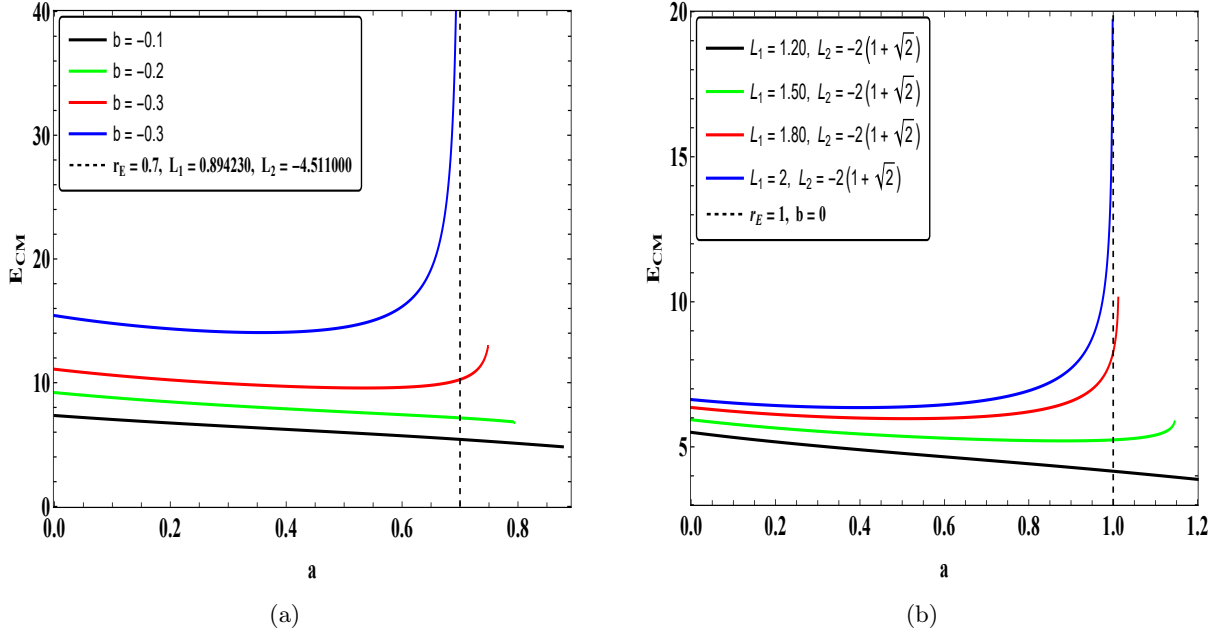


Figure 10: Variation of the center-of-mass energy E_{CM} versus the spin parameter a . Panel (a) shows the EMDA case for different values of the dilaton parameter b , while panel (b) corresponds to the extremal Kerr black hole limit ($b = 0$). In both panels, the vertical line indicates the location of the event horizon.

$$\frac{E_{CM}^2}{2M_0^2} \Big|_{r \rightarrow r_H^+} = \frac{1}{K(L_3 - L'_c)(L_4 - L'_c)} \left(\alpha_0 + L_4(\alpha_1 L_4 + \alpha_2 L_3 + \alpha_1) + L_3(\alpha_2 L_3 + \alpha_1 L_4 + \alpha_3) \right), \quad (59)$$

with coefficients

$$K(b, a) = \frac{r_H^+(2b + r_H^+)}{a^2 + r_H^+(-2b + r_H^+ - 2)},$$

$$\alpha_0 = 2r_H^+(2b + r_H^+)(r_H^+ - 1)(2b + r_H^+), \quad \alpha_1 = -2a(2b + 1),$$

$$\alpha_2 = (2b - r_H^+ + 2), \quad \alpha_3 = 2a^2(4b + r_H^+ + 1).$$

By substituting $b = -0.3$, $a = 0.55$ and $r_H^+ = 1.12$ (see Table 8) into the above expression, Eq. (59) reads as

$$\frac{E_{CM}^2}{2M_0^2} \Big|_{r \rightarrow r_H^+} = \frac{1}{0.000213(L_3 - L'_c)(L_4 - L'_c)} \left(0.2756 + L_4(-0.84L_4 + 0.4127L_3 - 0.768) \right. \\ \left. + L_3(0.4127L_3 - 0.84L_4 + 1.3596) \right), \quad (60)$$

where $L'_c = \frac{E}{\Omega_H} = 1.61$ and according to Eq. (60), one might expect that the center-of-mass energy E_{CM} can diverge when either L_3 or L_4 equals the critical angular momentum L'_c . Nevertheless, for such a divergence to occur physically, the particle with angular momentum L'_c must be capable of reaching

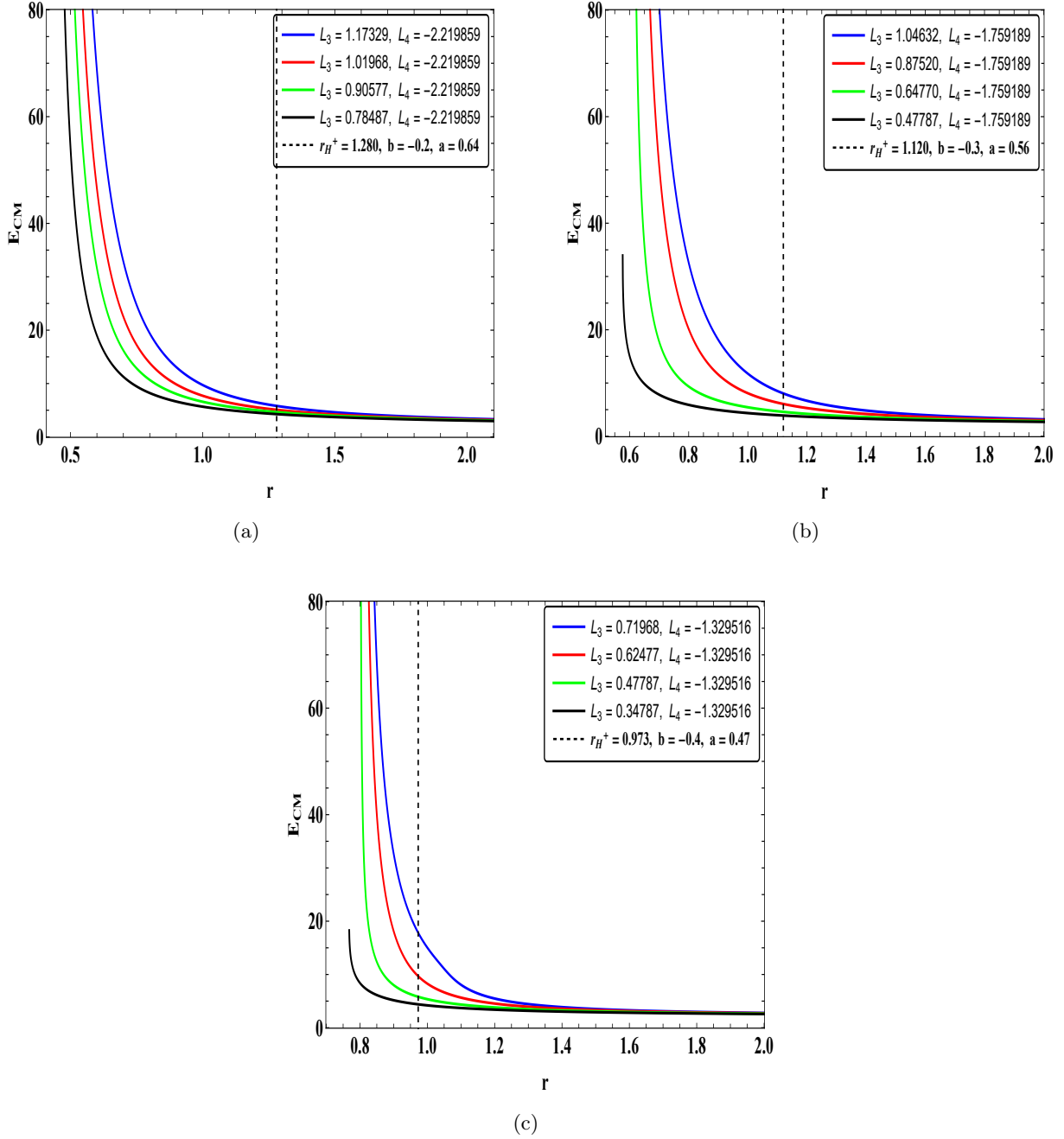


Figure 11: Variation of the center-of-mass energy E_{CM} versus radial coordinate r for a non-extremal EMDA black hole for fixed values of the dilaton parameter $b = -0.2$, $b = -0.3$ and $b = -0.4$, respectively. Each curve corresponds to different values of the angular momentum L_3 , with L_4 held constant. The vertical dashed line in each plot denotes the location of the outer event horizon r_+ of the EMDA black hole.

the event horizon. In other words, L'_c should lie within the permissible range of angular momenta that allow the particle to fall into the black hole and participate in a collision near the horizon. As shown in Table (8), for the parameter set $b = -0.3$ and $a = 0.55$, the allowed range of angular momentum is $L_3 < L < L_4$. It is evident that L'_c does not lie within this range; rather, it satisfies $L'_c > L_4$. This indicates that, in the case of a non-extremal EMDA black hole, a particle with angular momentum $L = L'_c$ is unable to reach the event horizon or fall into the black hole. Consequently, E_{CM} for the non-extremal configuration possesses a finite maximum value. Figure (11) illustrates the near-horizon variation of the center-of-mass energy, E_{CM} , as a function of the radial coordinate r for different

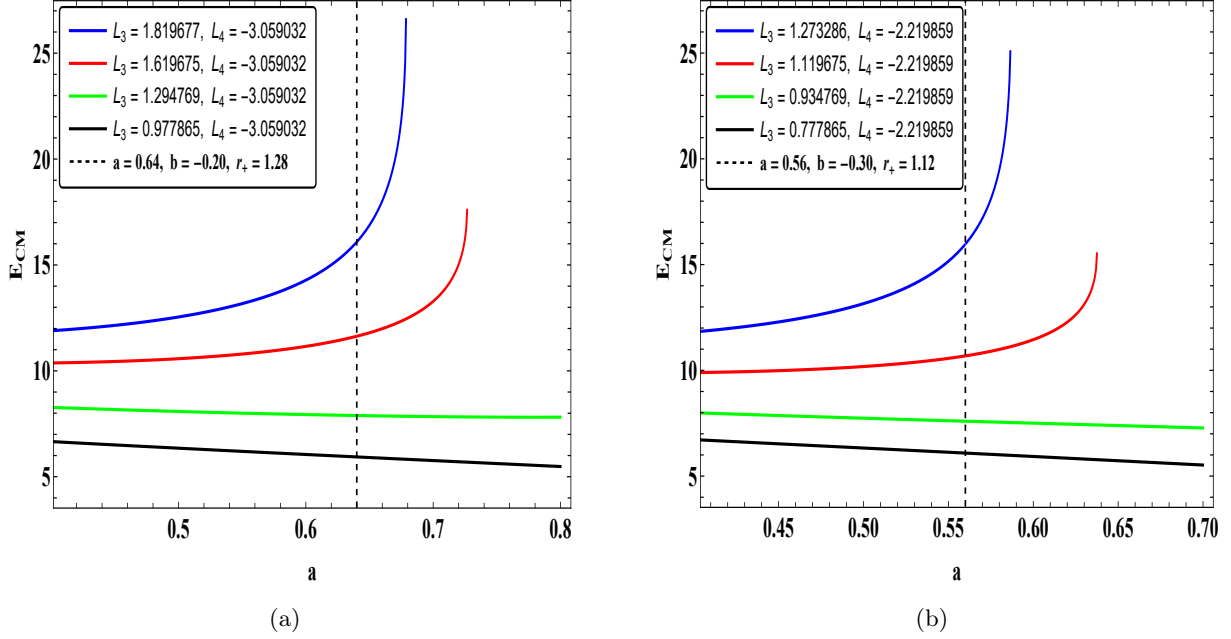


Figure 12: Variation of the center-of-mass energy E_{CM} versus the spin parameter a for a non-extremal EMDA black hole for fixed values of the dilaton parameter $b = -0.2$ and $b = -0.3$, respectively. Each curve corresponds to different values of the angular momentum L_3 , with L_4 held constant. The vertical dashed line in each plot denotes the location of the outer event horizon r_+ of the EMDA black hole.

choices of L_3 and L_4 , with the parameters a and b fixed at selected combinations, for a non-extremal EMDA black hole. Figure (12) presents the corresponding dependence of E_{CM} on the spin parameter a for different values of L_3 and L_4 , with the dilaton parameter b kept fixed.

7 Discussion & Summary

Singularities are predicted to develop in classical GR by the famous singularity theorems. Spacetime singularities, however, are generally thought to be a construct or restriction of the conventional GR rather than an occurrence in nature. More focus is being placed on phenomenological approaches to try to address the singularity problem in classical GR and explore any potential ramifications because we do not yet have a well-defined theory of quantum gravity. To understand the inside of a black hole, it is crucial to study classical black holes and their effects that have regular, or nonsingular, features. In accordance with the no-hair theorem, astrophysical black holes are theoretically expected to be fully described by the Kerr solution within the framework of GR. Nonetheless, whether this idealised description accurately reflects the nature of real astrophysical black holes remains an open and significant question. Therefore, we repeatedly consider black holes beyond the Kerr family as theoretical extensions that can provide crucial tests and possible evidence for deviations from the Kerr paradigm.

The spacetime we investigated in this paper, equipped with all its field content, is a rotating EMDA black hole. Within this context, the role of the dilaton parameter b becomes crucial. Its influence on critical spacetime features such as the event horizon structure, the ergoregion, and the dynamics of particle acceleration provides a compelling theoretical basis for differentiating rotating EMDA black holes from their Kerr counterparts. A detailed analysis of these deviations offers a promising avenue for testing the validity of GR in strong gravitational regimes and for assessing the true nature of astrophysical black hole candidates. In view of this, we have examined the characteristics of horizons

created by the stationary EMDA black hole and explicitly highlighted the influence of the dilaton parameter b . The analysis was extended to energy extraction through the Penrose process, revealing the impact of the dilaton parameter on the efficiency of energy extracted from the black hole. The Penrose process provides a general picture of the energy acquired by a particle orbiting the black hole, but determining how much of that truly corresponds to the black hole's rotational energy is far more difficult. To answer this question, we have investigated the initial mass energy extracted from the EMDA black hole and presented our findings. Furthermore, we have examined the minimum velocity range of the local disintegrating fragments required for energy extraction and superradiance. We have investigated the possibility of the superradiance and calculated the energy flux lost per unit time, along with the angular velocity at the horizon. Thus, this gives us the idea of the dependency of the dilaton parameter on the energy flux that radiates out from the black hole.

The essential conclusions emerging from our investigations can be outlined as follows.

- (i) The structure of the horizon for this nontrivial spacetime has been analysed to determine the critical (or extremal) values of the parameters $a = a_E$ and b , which characterise the condition for the existence of an extremal black hole with a degenerate horizon. These extremal values define a boundary that clearly separates the black hole regime from that of an NS in the parameter space. In addition, we have also examined the allowed range of the parameter b corresponding to physically meaningful (positive) values of the radial coordinate r . Finally, we extended our analysis to illustrate the boundary that distinguishes a black hole from an NS using the $b - a$ parameter space diagram.
- (ii) The equations of motion governing the energy extraction processes have been derived and analysed accordingly. The most striking results emerge when the parameter b takes on increasingly negative values in the case of an extremal black hole. Under such conditions, the Penrose process is found to be significantly more efficient, reaching up to approximately 91% compared to that in a Kerr black hole or any other member of the Kerr family. Furthermore, it is shown that through the Penrose process, it is possible to extract nearly 62.6% of the initial mass of an extremal black hole in this scenario.
- (iii) Next, we examined the Wald inequality for this spacetime. Unlike the Kerr black hole, the EMDA extremal EMDA black hole satisfies $a_E = r_E = 1 + b$, so both the extremal spin and the horizon radius decrease linearly with negative b . Kinematically, the Wald bound on the local fragment speed at the horizon is relaxed in the case of EMDA spacetime, i.e., $|v|_{\min}$ decreases monotonically as b becomes more negative—by $\sim 6.5\%$ at $b = -0.1$, $\sim 18.4\%$ at $b = -0.2$, and 50% at $b = -0.3$ relative to Kerr case. Consequently, although EMDA spacetime tightens the extremal spin ceiling ($a_E = 1 + b$), it simultaneously lowers the threshold for horizon crossing negative energy influx set by Wald, rendering energy extraction processes more permissive for the same mass scale.
- (iv) Furthermore, with the Bardeen-Press-Teukolsky inequality, we find that a negative dilaton parameter b linearly reduces the extremal spin and horizon radius ($a_E = r_E = 1 + b$), and concomitantly lowers the near-horizon kinematic thresholds relative to Kerr, i.e., $|v|_{\min}$ decreases by $\sim 8.8\%$ ($b = -0.1$), 23.3% ($b = -0.2$), and 55.9% ($b = -0.3$), while $|v|_{\text{rel}}$ drops by $\sim 6.5\%$, 18.4% , and 50.0% , respectively. Finally, EMDA black hole enforces a tighter global spin bound (smaller a_{max}) yet a more permissive local Wald threshold, thereby facilitating horizon-crossing energy extraction despite a reduced extremal parameter space.
- (v) The superradiant scattering phenomenon in the EMDA spacetime is significantly stronger than in the Kerr geometry due to the influence of the dilaton charge b . Negative values of b reduce the horizon radius and enhance the horizon angular velocity Ω_H , thereby widening the superradiant

frequency window $\omega_m \Omega_H < 0$, and deepening the energy-flux minimum. Consequently, EMDA black hole allows more efficient extraction of rotational energy, particularly near extremality, illustrating that string-inspired corrections can amplify superradiant phenomena beyond the limits of the classical Kerr solution.

- (vi) We compute the effective potential and, by imposing the circular-geodesic conditions $\dot{r} = 0$ and $\partial_r V_{\text{eff}} = 0$ (with stability assessed via $\partial_r^2 V_{\text{eff}}$), determine the corresponding range of angular momentum. Further, from the behaviour of \dot{r} as a function of r , we identify the critical angular momentum L_c for which the radial motion remains allowed all the way down to the event horizon, ensuring that the colliding particles can indeed reach the black hole horizon. Lastly, using these conserved quantities, we compute the centre-of-mass energy E_{CM} of the collision.
- (vii) Finally, we have analysed the centre-of-mass energy E_{CM} of particle collisions near rotating EMDA black holes, explicitly demonstrating how the dilaton parameter b governs the collision energetics. The BSW mechanism is found to depend simultaneously on the rotation parameter a and the dilaton parameter b . While the formalism smoothly reduces to the Kerr black hole case in the limit $b \rightarrow 0$, negative values of b modify the horizon structure, angular velocity, and critical angular momentum without destroying the BSW mechanism. For extremal EMDA black holes, E_{CM} diverges when one of the colliding particles attains the critical angular momentum, indicating that such spacetimes can, in principle, act as natural particle accelerators. In contrast, for non-extremal EMDA black holes, the critical angular momentum lies outside the physically admissible range, ensuring that the centre-of-mass energy remains finite. These results establish the dilaton field as a key regulator of high-energy collision processes in EMDA spacetimes, clarifying the conditions under which ultra-high-energy particle interactions may arise in strong-gravity regimes.

Acknowledgments

AKC gratefully acknowledges Parthapratim Pradhan for valuable discussions on energy extraction and particle acceleration in general relativity. His suggestions, particularly regarding the geometric formulation of the Penrose process, as well as his comments on early drafts, helped improve the clarity and presentation of this work. AKC also acknowledges the facilities at ICARD, Gurukula Kangri (Deemed to be University), Haridwar, India.

References

- Abbasi, K. Q., Carneiro, F. L., and Moughal, M. Z. A. (2025). Energy extraction from rotating black hole with quintessential energy through the penrose process.
- Abdujabbarov, A., Ahmedov, B., and Ahmedov, B. (2011a). Energy extraction and particle acceleration around a rotating black hole in hořava-lifshitz gravity. *Phys. Rev. D*, 84:044044.
- Abdujabbarov, A. A., Ahmedov, B. J., Shaymatov, S. R., and Rakhmatov, A. S. (2011b). Penrose process in kerr-taub-nut spacetime. *Astrophysics and Space Science*, 334(2):237-241.
- Amir, M., Ahmed, F., and Ghosh, S. G. (2016). Collision of two general particles around a rotating regular hayward’s black holes. *The European Physical Journal C*, 76(10).
- Amir, M. and Ghosh, S. G. (2015). Rotating Hayward’s regular black hole as particle accelerator. *JHEP*, 07:015.
- Bañados, M., Silk, J., and West, S. M. (2009). Kerr black holes as particle accelerators to arbitrarily high energy. *Phys. Rev. Lett.*, 103:111102.

- Bardeen, J. M., Press, W. H., and Teukolsky, S. A. (1972). Rotating Black Holes: Locally Nonrotating Frames, Energy Extraction, and Scalar Synchrotron Radiation. *Astrophysical Journal*, 178:347–370.
- Battista, E. (2024). Quantum Schwarzschild geometry in effective field theory models of gravity. *Physical Review D*, 109(2):026004.
- Bekenstein, J. D. (1973). Extraction of energy and charge from a black hole. *Phys. Rev. D*, 7:949–953.
- Bekenstein, J. D. and Schiffer, M. (1998). The many faces of superradiance. *Phys. Rev. D*, 58(6):064014.
- Bhat, M., Dhurandhar, S., and Dadhich, N. (1985). Energetics of the Kerr-Newman Black-Hole by the Penrose Process. *Journal of Astrophysics and Astronomy*, 6(2):85–100.
- Blázquez-Salcedo, J. L., Herdeiro, C., Radu, E., dos Santos Costa Filho, E., and Uzawa, K. (2025). Spinning extremal dyonic black holes in $\gamma = 1$ Einstein-Maxwell-dilaton theory. *arXiv e-prints*, arXiv:2512.20698 [gr-qc].
- Brito, R., Cardoso, V., and Pani, P. (2020). *Superradiance: New Frontiers in Black Hole Physics*. Springer International Publishing.
- Carroll, S. M. (2019). *Spacetime and Geometry: An Introduction to General Relativity*. Cambridge University Press.
- Chandrasekhar, S. (1983). The mathematical theory of black holes. *Oxford University Press New York*.
- Chatterjee, A. K. and Pradhan, P. (2026). Inertial frame dragging as a probe to differentiate Kerr-Newman naked singularities from black holes. *arXiv e-prints*, arXiv:2602.18972.
- Chen, H., Xu, H., Zhan, Y., and Zhang, S.-J. (2025). Electric penrose process in ayón-beato-garcía (-ds) black holes.
- Chen, S. and Jing, J. (2013). Gravitational field of a slowly rotating black hole with a phantom global monopole. *Class. Quant. Grav.*, 30:175012.
- Cheriyodathillathu, V., Das, S., and Basak, S. (2025). Superradiance of anyons. *International Journal of Modern Physics D*, 34(14).
- Christodoulou, D. (1970). Reversible and irreversible transformations in black-hole physics. *Phys. Rev. Lett.*, 25:1596–1597.
- Christodoulou, D. and Ruffini, R. (1971). Reversible transformations of a charged black hole. *Phys. Rev. D*, 4:3552–3555.
- Dos Santos Costa Filho, E. (2025). From Rotating Attractors to Extremal Black Holes with Axionic Hair. *arXiv e-prints*, arXiv:2601.00066 [gr-qc].
- Fatima, U. and Abbas, G. (2025). Revisiting the penrose process in rotating black holes with quantum corrections: Implications for energy extraction and irreducible mass.
- Feiteira, D., Lemos, J. P. S., and Zaslavskii, O. B. (2025). Penrose and super-penrose energy extraction from a reissner-nordström black hole spacetime with a cosmological constant through the bañados-silk-west mechanism. *Phys. Rev. D*, 111:024022.
- Flathmann, K. and Grunau, S. (2015a). Analytic solutions of the geodesic equation for einstein-maxwell-dilaton-axion black holes. *Physical Review D*, 92(10).

- Flathmann, K. and Grunau, S. (2015b). Analytic solutions of the geodesic equation for Einstein-Maxwell-dilaton-axion black holes. *Phys. Rev. D*, 92(10):104027.
- Flathmann, K. and Grunau, S. (2016). Analytic solutions of the geodesic equation for U (1) 2 dyonic rotating black holes. *Physical Review D*, 94(12):124013.
- Ganguly, C. and SenGupta, S. (2014). Penrose process in charged axion-dilaton coupled black hole.
- García, A., Galtsov, D., and Kechkin, O. (1995). Class of stationary axisymmetric solutions of the einstein-maxwell-dilaton-axion field equations. *Phys. Rev. Lett.*, 74:1276–1279.
- Ghosh, A. and Mitra, P. (1994). Entropy in dilatonic black hole background. *Physical Review Letters*, 73(19):2521-2523.
- Ghosh, S. G. and Sheoran, P. (2014). Higher dimensional non-kerr black hole and energy extraction. *Phys. Rev. D*, 89:024023.
- Ghosh, S. G., Sheoran, P., and Amir, M. (2014). Rotating ayón-beato-garcía black hole as a particle accelerator. *Phys. Rev. D*, 90:103006.
- Gupta, K., Law, Y. T. A., and Levin, J. (2021). Penrose process for a charged black hole in a uniform magnetic field. *Phys. Rev. D*, 104:084059.
- Ha, Y. K. (2007). A new theorem for black holes.
- Harada, T. and Kimura, M. (2014). Black holes as particle accelerators: a brief review. *Classical and Quantum Gravity*, 31(24):243001.
- Hawking, S. W. (1975). Particle Creation by Black Holes. *Commun. Math. Phys.*, 43:199–220. [Erratum: *Commun.Math.Phys.* 46, 206 (1976)].
- Herdeiro, C., Radu, E., and dos Santos Costa Filho, E. (2025). Charged, rotating black holes in Einstein-Maxwell-dilaton theory. *arXiv e-prints*, arXiv:2506.15798 [gr-qc].
- Herrero-Valea, M. and Simon-Felix, E. (2024). Superradiant scattering in lorentz-violating gravity.
- Hussain, I. (2012). Black Holes and Collision Energy in the Center-Of Frame. *Modern Physics Letters A*, 27(12):1250068–1–1250068–10.
- Jacobson, T. and Sotiriou, T. P. (2010). Spinning black holes as particle accelerators. *Phys. Rev. Lett.*, 104:021101.
- Jha, S. K. (2024). Superradiance scattering of electromagnetic and gravitational fields and thin accretion disk around non-commutating kerr black hole. *The European Physical Journal C*, 84(11).
- Jing, J.-L. (1996). Thermodynamics of stationary axisymmetric Einstein-Maxwell dilaton-axion black hole. *Nucl. Phys. B*, 476:548–555.
- Landsman, K. (2022). Penrose’s 1965 singularity theorem: from geodesic incompleteness to cosmic censorship. *Gen. Rel. Grav.*, 54(10):115.
- Liu, C., Chen, S., Ding, C., and Jing, J. (2011). Particle Acceleration on the Background of the Kerr-Taub-NUT Spacetime. *Phys. Lett. B*, 701:285–290.
- Liu, Q.-X., Hu, Y.-P., Sui, T.-T., and An, Y.-S. (2024). Superradiance of rotating black holes surrounded by dark matter. *Physics of the Dark Universe*, 46:101624.

- Mao, P.-J., Li, R., Jia, L.-Y., and Ren, J.-R. (2017). Acceleration of particles in einstein-maxwell-dilaton black holes. *Chinese Physics C*, 41(6):065101.
- Matarrese, S., Colpi, M., Gorini, V., and Moschella, U., editors (2011). *Dark Matter and Dark Energy: A Challenge for Modern Cosmology*, volume 370 of *Astrophysics and Space Science Library*.
- Menza, L. D. and Nicolas, J.-P. (2015). Superradiance on the reissner-nordström metric. *Classical and Quantum Gravity*, 32(14):145013.
- Mino, Y. (2003). Perturbative approach to an orbital evolution around a supermassive black hole. *Phys. Rev. D*, 67:084027.
- Mollicone, A. and Destounis, K. (2025). Superradiance of charged black holes embedded in dark matter halos. *Physical Review D*, 111(2).
- Mukherjee, S., Chakraborty, S., and Dadhich, N. (2019). On some novel features of the kerr-newman-nut spacetime. *The European Physical Journal C*, 79(2).
- Ovcharenko, H. V. and Zaslavskii, O. B. (2024a). High-energy head-on particle collisions near event horizons: Classification of scenarios. *International Journal of Modern Physics D*, 33(16).
- Ovcharenko, H. V. and Zaslavskii, O. B. (2024b). Near-horizon properties of trajectories with finite force relevant for bañados-silk-west effect. *Phys. Rev. D*, 110:064016.
- Pan, Q.-Y. and Jing, J.-L. (2007). Quasinormal frequencies and thermodynamic instabilities for the stationary axisymmetric Einstein-Maxwell dilaton-axion black hole. *JHEP*, 01:044.
- Pani, P., Cardoso, V., Gualtieri, L., Berti, E., and Ishibashi, A. (2012). Black-hole bombs and photon-mass bounds. *Phys. Rev. Lett.*, 109:131102.
- Parthasarathy, S., Wagh, S. M., Dhurandhar, S. V., and Dadhich, N. (1986a). High Efficiency of the Penrose Process of Energy Extraction from Rotating Black Holes Immersed in Electromagnetic Fields. *Astrophysical Journal*, 307:38.
- Parthasarathy, S., Wagh, S. M., Dhurandhar, S. V., and Dadhich, N. (1986b). High Efficiency of the Penrose Process of Energy Extraction from Rotating Black Holes Immersed in Electromagnetic Fields. *Astrophysical Journal*, 307:38.
- Patil, M. and Joshi, P. S. (2011). Kerr naked singularities as particle accelerators. *Class. Quantum Grav.*, 28(23):235012.
- Patil, M., Joshi, P. S., and Malafarina, D. (2011). Naked singularities as particle accelerators. ii. *Phys. Rev. D*, 83(6):064007.
- Pengpan, T. (2025). Superradiance and quasinormal modes of massive scalar fields around kerr black holes in einstein-maxwell-dilaton-axion theory with perfect fluid dark matter.
- Penrose, R. (1965). Gravitational collapse and space-time singularities. *Phys. Rev. Lett.*, 14(3):57–59.
- Penrose, R. and Floyd, R. M. (1971). Extraction of rotational energy from a black hole. *Nature*, 229:177–179.
- Planck Collaboration, Ade, P. A. R., Aghanim, N., Armitage-Caplan, C., Arnaud, M., et al. (2014). Planck 2013 results. XVI. Cosmological parameters. *Astronomy & Astrophysics*, 571:A16.
- Pradhan, P. (2014). Regular black holes as particle accelerators.

- Pradhan, P. (2019). Study of energy extraction and epicyclic frequencies in kerr-mog (modified gravity) black hole. *The European Physical Journal C*, 79(5).
- Press, W. H. and Teukolsky, S. A. (1972). Floating Orbits, Superradiant Scattering and the Black-hole Bomb. *Nature*, 238:211–212.
- Rubin, V. C., Ford, Jr., W. K., and Thonnard, N. (1980). Rotational properties of 21 SC galaxies with a large range of luminosities and radii, from NGC 4605 (R=4kpc) to UGC 2885 (R=122kpc). *Astrophysical Journal*, 238:471–487.
- Rudra, A., Nandan, H., Gannouji, R., Chakraborty, S., and Chatterjee, A. K. (2020). Rotating dyonic black hole in $N = 2, U(1)^2$ gauged supergravity as natural laboratory for high energy particle collisions. *Class. Quant. Grav.*, 37(22):225010.
- Senovilla, J. M. M. and Garfinkle, D. (2015). The 1965 Penrose singularity theorem. *Class. Quant. Grav.*, 32(12):124008.
- Sharma, P., Nandan, H., Papnoi, U., and Chatterjee, A. K. (2021). Optical and thermodynamic properties of a rotating dyonic black hole spacetime in $\mathcal{N} = 2, U(1)^2$ gauged supergravity. *Eur. Phys. J. C*, 81:429.
- Sheoran, P. et al. (2020). Schwarzschild black hole surrounded by quintessential matter field as an accelerator for spinning particles. *Phys. Rev. D*, 102(6):064046.
- Thorne, K. S. (1974). Disk-Accretion onto a Black Hole. II. Evolution of the Hole. *Astrophysical Journal*, 191:507–520.
- Viththani, D. P., Bhanja, T., Patel, V., and Joshi, P. S. (2024). Magnetic penrose process and kerr black hole mimickers. *Phys. Rev. D*, 110:123035.
- Wald, R. M. (1974). Energy Limits on the Penrose Process. *Astrophysical Journal*, 191:231–234.
- Wang, Z.-L. and Battista, E. (2025). Dynamical features and shadows of quantum Schwarzschild black hole in effective field theories of gravity. *European Physical Journal C*, 85(3):304.
- Wei, S.-W. and Liu, Y.-X. (2013). Observing the shadow of einstein-maxwell-dilaton-axion black hole. *Journal of Cosmology and Astroparticle Physics*, 2013(11):063-063.
- Wei, S.-W., Liu, Y.-X., Guo, H., and Fu, C.-E. (2010). Charged spinning black holes as particle accelerators. *Phys. Rev. D*, 82:103005.
- Yoshino, H. and Kodama, H. (2012). Bosenova collapse of axion cloud around a rotating black hole. *Progress of Theoretical Physics*, 128(1):153-190.
- Zakria, A. and Jamil, M. (2015). Center of Mass Energy of the Collision for Two General Geodesic Particles Around a Kerr-Newman-Taub-NUT Black Hole. *JHEP*, 05:147.
- Zaslavskii, O. B. (2010). Acceleration of particles by nonrotating charged black holes? *JETP Letters*, 92(9):571-574.
- Zaslavskii, O. B. (2023). The bañados-silk-west effect with immovable particles near static black holes and its rotational counterpart. *Gravitation and Cosmology*, 29(1):74-78.
- Zhang, S.-J. (2025). Penrose process in magnetized non-kerr rotating spacetime with anomalous quadrupole moment. *Journal of Cosmology and Astroparticle Physics*, 2025(12):004.
- Zwicky, F. (2009). Republication of: The redshift of extragalactic nebulae. *General Relativity and Gravitation*, 41(1):207–224.